

## oMEGACat. IX. Chemical Tagging of Omega Centauri Populations with Machine-Learning-Inferred Abundances from the MUSE Spectrograph

Z. WANG (王梓先) <sup>1</sup>, A. C. SETH <sup>1</sup>, C. CLONTZ <sup>1,2</sup>, N. NEUMAYER <sup>2</sup>, M. HÄBERLE <sup>3</sup>, S. KAMANN <sup>4</sup>,  
M. LATOUR <sup>5</sup>, M. S. NITSCHAI <sup>2</sup>, P. J. SMITH <sup>2,6</sup>, S. O. SOUZA <sup>2</sup>, M. ALFARO-CUELLO <sup>7</sup>, A. BELLINI <sup>8</sup>,  
A. FELDMEIER-KRAUSE <sup>9</sup>, N. KACHAROV <sup>10</sup>, M. LIBRALATO <sup>11</sup>, A. P. MILONE <sup>12,13</sup> AND G. VAN DE VEN <sup>9</sup>

<sup>1</sup>*Department of Physics and Astronomy, University of Utah, Salt Lake City, UT 84112, USA*

<sup>2</sup>*Max Planck Institute for Astronomy, Königstuhl 17, D-69117 Heidelberg, Germany*

<sup>3</sup>*European Southern Observatory, Karl-Schwarzschild-Strae 2, 85748 Garching, Germany*

<sup>4</sup>*Astrophysics Research Institute, Liverpool John Moores University, 146 Brownlow Hill, Liverpool L3 5RF, UK*

<sup>5</sup>*Institut für Astrophysik und Geophysik, Georg-August-Universität Göttingen, Friedrich-Hund-Platz 1, 37077 Göttingen, Germany*

<sup>6</sup>*Fakultät für Physik und Astronomie, Universität Heidelberg, Im Neuenheimer Feld 226, D-69120 Heidelberg, Germany*

<sup>7</sup>*Centro de Investigación en Ciencias del Espacio y Física Teórica, Universidad Central de Chile, La Serena 1710164, Chile*

<sup>8</sup>*Space Telescope Science Institute, 3700 San Martin Dr., Baltimore, MD, 21218, USA*

<sup>9</sup>*Department of Astrophysics, University of Vienna, Türkenschanzstrasse 17, 1180 Wien, Austria*

<sup>10</sup>*Leibniz Institute for Astrophysics, An der Sternwarte 16, 14482 Potsdam, Germany*

<sup>11</sup>*INAF - Osservatorio Astronomico di Padova, Vicolo dell'Osservatorio 5, Padova I-35122, Italy*

<sup>12</sup>*Dipartimento di Fisica e Astronomia "Galileo Galilei", Università di Padova, Vicolo dell'Osservatorio 3, Padova, IT-35122*

<sup>13</sup>*Istituto Nazionale di Astrofisica - Osservatorio Astronomico di Padova, Vicolo dell'Osservatorio 5, Padova, IT-35122*

(Received XX; Revised XX; Accepted XX)

Submitted to APJ

### ABSTRACT

We present chemical abundance measurements for 7,302 red giant branch stars within the half-light radius ( $\sim 5'$ ) of  $\omega$  Centauri ( $\omega$  Cen), derived from MUSE spectra using the neural network model DD-PAYNE. DD-PAYNE effectively identifies spectral features of C, N, and O for  $[\text{Fe}/\text{H}] > -1.0$  dex; Mg for  $[\text{Fe}/\text{H}] > -1.5$  dex; and Na, Ca, and Ba for all metallicities. By combining these measurements with previous high-resolution studies, we create the most comprehensive picture of  $\omega$  Cen's rich chemical evolutionary history. For the first time, we map elemental variations across the entire chromosome diagram, which is widely used to identify multiple populations. We analyze the median chemical abundance trends as functions of age and metallicity for different subpopulations. The DD-PAYNE measurements of  $[\text{C}/\text{Fe}]$ ,  $[\text{N}/\text{Fe}]$ , and  $[\text{O}/\text{Fe}]$  extend literature trends to higher metallicities and show continuous abundance-metallicity relations, with  $[(\text{C}+\text{N}+\text{O})/\text{Fe}]$  increasing steadily with  $[\text{Fe}/\text{H}]$ .  $[\text{Ca}/\text{Fe}]$  and the *s*-process element  $[\text{Ba}/\text{Fe}]$  also increase with metallicity across all populations. For  $[\text{Ba}/\text{Fe}]$ , the chemically enhanced (P2) populations are more enriched than primordial (P1) and the intermediate (Im) populations. Furthermore,  $[\text{N}/\text{Fe}]$  correlates strongly with stellar age while  $[\text{Ca}/\text{Fe}]$  and  $[\text{Ba}/\text{Fe}]$  exhibits a weaker age dependence. Using these abundance-metallicity-age relations, we evaluate different formation scenarios of  $\omega$  Cen proposed in the literature. Our study demonstrates that combining MUSE with machine learning enables large-sample stellar abundance measurements in crowded cluster cores, overcoming the limitations of fiber-fed spectroscopy for studying multiple stellar populations and their evolutionary histories.

**Keywords:** Globular star clusters (656) — Galaxy nuclei (609) — Star clusters (1567) — Chemical abundances (224) — Stellar populations (1622)

### 1. INTRODUCTION

Omega Centauri ( $\omega$  Cen; NGC 5139), the most massive stripped nuclear star cluster (NSC) in the Milky

Way, remains one of the most challenging stellar systems to unravel in terms of its formation and evolution. Unlike typical mono-metallic globular clusters,  $\omega$  Cen exhibits a large metallicity spread of  $> 1$  dex (e.g., K. C. Freeman & A. W. Rodgers 1975; J. E. Norris & G. S. Da Costa 1995; C. I. Johnson & C. A. Pilachowski 2010; M. S. Nitschai et al. 2024) and hosts multiple stellar populations (e.g., L. R. Bedin et al. 2004; A. Bellini et al. 2017; M. Latour et al. 2021; C. Clontz et al. 2025a) with distinct chemical abundance patterns (e.g., J. E. Norris & G. S. Da Costa 1995; L. Origlia et al. 2003; A. F. Marino et al. 2011; R. G. Gratton et al. 2011). An intermediate-mass black hole (IMBH) has also been recently confirmed in  $\omega$  Cen through the detection of fast-moving stars (M. Häberle et al. 2024a), further supporting its origin as the stripped nucleus of an accreted dwarf galaxy (e.g., K. Bekki & K. C. Freeman 2003; T. Tsuchiya et al. 2003; M. Ideta & J. Makino 2004; S. R. Majewski et al. 2012). All these features point to a highly complex formation history of  $\omega$  Cen, which therefore makes it a key system both for understanding the formation of nuclear star clusters (N. Neumayer et al. 2020) and the assembly history of the Milky Way (e.g., M. Xiang & H.-W. Rix 2022).

Decades of photometric studies have characterized  $\omega$  Cen’s multiple populations. Early observations found multiple sequences in the cluster’s color-magnitude diagram (e.g., J. Norris & M. S. Bessell 1975; Y.-W. Lee et al. 1999; E. Pancino et al. 2000; F. R. Ferraro et al. 2004). Notably,  $\omega$  Cen hosts a split main-sequence, with a blue branch that is more helium-rich (and slightly more metal-rich) than the red branch (L. R. Bedin et al. 2004; G. Piotto et al. 2005; I. R. King et al. 2012; M. Latour et al. 2021). In recent years, Hubble Space Telescope (*HST*) multi-band photometry has enabled the construction of “chromosome diagrams”; pseudo-color-color diagrams that disentangle multiple stellar populations within star clusters based on variations in light elements (He, N, O) (e.g., L. Sbordone et al. 2011; A. P. Milone et al. 2017a,b; A. F. Marino et al. 2019). The chromosome map of  $\omega$  Cen reveals at least three primary populations separated vertically in the diagram. On the bottom are stars with field-like abundances, a.k.a., P1 or first-generation stars. Enriched stars fall on top two separate sequences, an intermediate and upper sequence (Im and P2 hereafter) that are also often referred to as second-generation stars (M. S. Nitschai et al. 2024; C. Clontz et al. 2025b; A. C. Mason et al. 2025; E. Donoghio et al. 2026). A more detailed analysis of the chromosome diagram with the application of clustering algorithms also revealed that these primary groups of stars can be further divided into  $\sim 15$  subpopulations (A.

Bellini et al. 2017; C. Clontz et al. 2025a). These photometric subpopulations indicate the presence of multiple episodes of star formation and chemical enrichment within  $\omega$  Cen.

Early analysis of sub-giant branch (SGB) stars suggested a prolonged star formation history, with the inferred age spread ranging from 2 to 4 Gyr (e.g., L. M. Stanford et al. 2006; S.-J. Joo & Y.-W. Lee 2013; S. Villanova et al. 2014; M. Tailo et al. 2016). C. Clontz et al. (2024) combined metallicity and photometry for 8100 SGB stars (M. S. Nitschai et al. 2023; M. Häberle et al. 2024b), with new isochrones that include the impact of helium and C+N+O to construct a high-precision age-metallicity relation with most stars ranging in age from 10 to 13 Gyr. They resolved two distinct formation sequences, with a tighter, lower metallicity sequence and a more diffuse, higher metallicity population. By combining these age measurements with subpopulation clustering, C. Clontz et al. (2025a) found that P2 stars are  $\sim 1$  Gyr younger than P1 stars, with the Im population falling in between.

Spectroscopic studies have provided direct chemical abundance measurements and confirmed their complex variations in  $\omega$  Cen. One of the most striking deviations of  $\omega$  Cen is its extreme helium enrichment. A population with  $Y \simeq 0.39 - 0.44$  has been identified in contrast to the primordial helium population ( $Y \simeq 0.22$ ) (A. K. Dupree et al. 2011; A. K. Dupree & E. H. Avrett 2013; B. P. Hema & G. Pandey 2014; B. P. Hema et al. 2018, 2020; C. Clontz et al. 2025b). C. Clontz et al. (2025b) confirmed that these helium-enriched stars correspond directly to the P2 population on the chromosome diagram. Notably, significant helium enrichment is observed even at the lowest metallicities. In terms of light elements,  $\omega$  Cen exhibits the classical anti-correlations observed in many globular clusters, but with unique characteristics. High-resolution spectroscopic surveys have mapped a Na-O anti-correlation across all metallicities (C. I. Johnson & C. A. Pilachowski 2010; A. F. Marino et al. 2011), along with an Mg-Al anti-correlation that is particularly extended in the metal-poor and intermediate populations (S. Mészáros et al. 2021; D. A. Alvarez Garay et al. 2024). Furthermore, measurements of C, N, and O have revealed a pattern that is distinct from the constant C+N+O sum typically found in mono-metallic clusters (e.g., S. Mészáros et al. 2020). A. F. Marino et al. (2011, 2012) found that the total  $[(C+N+O)/Fe]$  abundance increases by approximately 0.5 dex from the most metal-poor component to the metal-rich population, with similar values at the same metallicity in both P1 and P2 populations. Similarly, slow neutron capture (*s*-process) elements such

as Ba and La increase monotonically with metallicity to extremely high values (e.g. C. I. Johnson & C. A. Pilachowski 2010; A. F. Marino et al. 2011, 2012).

Despite the above detailed studies on  $\omega$  Cen’s multiple populations with age spread and abundance variations, the formation and evolution history of  $\omega$  Cen remain elusive and heavily debated. For example, E. Dondoglio et al. (2026) argued for a self-enrichment scenario based on a combination of enrichment patterns and the radial profiles of the P2 stars being consistently more concentrated than the P1 population. They suggest that P2 formed directly from the ejecta of P1 stars, and that the intermediate (Im) population formed later from the combined ejecta of both P1 and P2. In contrast, A. C. Mason et al. (2025) proposed a hierarchical assembly scenario based on chemical tagging with observations from APOGEE DR17 ( Abdurro’uf et al. 2022). They suggested that the Im population may instead originate from gas-rich globular clusters that spiraled into the main  $\omega$  Cen progenitor, triggering the starburst that produced the P2 population. Resolving these contradictory interpretations requires a direct linking of photometrically-identified populations with detailed ages and large samples of chemical abundance measurements. However, previous spectroscopic studies of  $\omega$  Cen have mostly relied on fiber-fed instruments (e.g., FLAMES, APOGEE), which suffer from contamination of the fiber light by adjacent stars in dense regions. As a result, detailed abundance analyses have been restricted to  $< 2000$  stars in the outskirts of  $\omega$  Cen, and even fewer when adopting the recommended quality cuts, leaving the inner regions ( $< 5'$ ) mostly unexplored.

The oMEGACat survey<sup>14</sup> overcomes these limitations by using the Multi Unit Spectroscopic Explorer (MUSE; R. Bacon et al. 2010), an integral-field spectrograph that can resolve individual stars within the crowded regions. This dataset provides over 300,000 MUSE stellar spectra within the half-light radius ( $\sim 5'$ ) of  $\omega$  Cen (M. S. Nitschai et al. 2023, 2024), with the wavelength covering 4750-9350 Å at moderate spectral resolution ( $R \sim 3000$ ). With the development of machine learning techniques for measuring chemical abundances from MUSE spectra (Z. Wang et al. 2022) and its successful demonstration on a globular cluster (R. Asa’d et al. 2024) and the inner Galaxy (Z. Wang et al. 2022, 2025a), we now have the opportunity to significantly expand the abundance measurements of  $\omega$  Cen. By obtaining a large number of abundances in  $\omega$  Cen’s inner regions, where oMEGACat multi-band photometry is available

(M. Häberle et al. 2024b), we can build the most comprehensive picture to date of abundance variations across  $\omega$  Cen’s multiple stellar populations.

In this paper, we apply the neural network model DATA-DRIVEN PAYNE (hereafter DD-PAYNE; Y.-S. Ting et al. 2017; M. Xiang et al. 2019) to measure the chemical abundances (C, N, O, Na, Mg, Ca, Ba) from MUSE spectra of  $\omega$  Cen. We then combine these measurements with literature abundance studies to investigate the chemical and age distributions of its stellar populations. We describe the oMEGACat dataset, selection criteria, and abundance measurement procedures in Section 2. In Section 3, we validate the reliability of the DD-PAYNE abundance measurements and compare them with high-resolution spectroscopic observations from the literature. We also outline the procedures to calibrate the DD-PAYNE abundances to the literature scale. Section 4 presents the abundance-metallicity relations and the abundance variations on the chromosome diagram. In Section 5, we examine the abundance differences and their relationships with metallicity, age, and subpopulation, including both the broader P1, Im, and P2 populations (C. Clontz et al. 2025b), and the more detailed subpopulations in C. Clontz et al. (2025a). We then combine our results and discuss potential formation scenarios of different populations in  $\omega$  Cen in Section 6. Finally, a summary of this work and directions for future studies is provided in Section 7.

## 2. DATA AND METHODS

### 2.1. oMEGACat and Quality Cuts

We use datasets from the oMEGACat project, which aims to disentangle the dynamics and formation history of  $\omega$  Cen by compiling the largest spectroscopic, photometric, and astrometric dataset to date. In brief, the data consists of two main catalogs covering  $\omega$  Cen within the half-light radius ( $\sim 5'$ ). The spectroscopic catalog is based on more than 100 MUSE pointings containing a total of 342,797 individual stellar spectra (M. S. Nitschai et al. 2023, hereafter N23). The *HST*-based catalog contains proper motions and seven-band photometry for up to  $\sim 1.4$  million stars (M. Häberle et al. 2024b, hereafter H24). These datasets have already enabled studies of the spatial metallicity distribution (M. S. Nitschai et al. 2024), the age-metallicity relation (C. Clontz et al. 2024), helium enrichment (C. Clontz et al. 2025b), 3D kinematics (M. Häberle et al. 2025), the foreground and internal gas kinematics (Z. Wang et al. 2025b), and have resulted in the identification of 14 stellar populations (C. Clontz et al. 2025a), and the discovery of a central intermediate-mass black hole (M. Häberle et al. 2024a). In this work, we use the stellar spectra from the

<sup>14</sup> <https://omegacatalog.github.io/>

oMEGACat MUSE catalog (N23) (containing 342,797 spectra) to estimate chemical abundances. We refer to N23 for details of the MUSE observations, data reduction, and spectra extraction.

We focus on red giant branch (RGB) stars in this study, due to their high signal-to-noise. RGB stars are also less affected by atomic diffusion, which can impact the abundance analyses in different populations (e.g., A. Dotter et al. 2017). Specifically, we apply the following selection criteria:

$$\begin{cases} P_M > 0.95 \\ m_{F625W} < 17 \text{ mag} \\ m_{F435W} - m_{F625W} > 1 \text{ mag} \\ \text{qflag}_{\text{PampelMUSE}} = 0 \\ S/N_{\text{MUSE}} > 50 \text{ pix}^{-1}, \end{cases} \quad (1)$$

where  $P_M$  is the membership probability of  $\omega$  Cen stars obtained from N23. The magnitude, color (both filters from J. Anderson & R. P. van der Marel 2010), and  $S/N_{\text{MUSE}}$  thresholds are used to select RGB stars with high-quality MUSE spectra. The PampelMUSE (S. Kamann et al. 2013) quality flag  $\text{qflag}_{\text{PampelMUSE}}$  further removes spectra with contributions from multiple sources, or source centroids located outside the data cube’s field of view. After applying these criteria, 7,346 stars remain in the sample; our final sample is a subsample of 7,302 of these stars after DD-PAYNE fitting quality cutoff, according to Section 2.2. A color-magnitude diagram (CMD) of the final sample is shown in the left panel of Fig. 1.

## 2.2. Measuring Chemical Abundances using DD-PAYNE

We apply the machine learning model DD-PAYNE (Y.-S. Ting et al. 2017; M. Xiang et al. 2019) to fit the MUSE spectra and measure chemical abundances. DD-PAYNE adopts the neural-network interpolator and fitting strategy of THE PAYNE (Y.-S. Ting et al. 2019) combined with physical gradient spectra from Kurucz spectral models (R. L. Kurucz 1970; R. Kurucz 1993; R. L. Kurucz 2005) to regularize the training process. The neural network model is trained on LAMOST spectra (G. Zhao et al. 2012; L.-C. Deng et al. 2012; X.-W. Liu et al. 2014, 2015) with stellar labels from high-resolution surveys, including GALAH DR2 (S. Buder et al. 2018) and APOGEE-PAYNE (Y.-S. Ting et al. 2019), and can derive  $T_{\text{eff}}$ ,  $\log g$ , micro-turbulence velocity ( $V_{\text{mic}}$ ), and 16 elemental abundances ( $[\text{Fe}/\text{H}]$  and  $[\text{X}/\text{Fe}]$  of C, N, O, Na, Mg, Al, Si, Ca, Ti, Cr, Mn, Co, Ni, Cu, and Ba) from LAMOST spectra (M. Xiang et al. 2019). A key advantage of DD-PAYNE is that it can enforce these stellar labels ( $T_{\text{eff}}$ ,  $\log g$ ,  $V_{\text{mic}}$ , and

abundances) to be measured physically from the spectral features, enabling its application to spectra from other instruments. We refer to M. Xiang et al. (2019) (hereafter X19) for more detailed descriptions of the training process and validation of DD-PAYNE. Z. Wang et al. (2022) applied DD-PAYNE to MUSE spectra and showed that several abundances (Fe, C, Mg, Si, Ti, Ni, Cr) can be measured with accuracies better than 0.1 dex. These results demonstrate that, despite line blending at low spectral resolution, models like DD-PAYNE can still provide reliable abundance measurements.

To measure chemical abundances from MUSE spectra of  $\omega$  Cen, we follow the procedures produced by Z. Wang et al. (2022). Briefly, we take the spectra from the oMEGACat MUSE observations (N23,  $R \sim 3000$ ) and degrade the spectral resolution to LAMOST ( $R \sim 1800$ ). Then we apply DD-PAYNE to fit the spectra in the wavelength region of 4750-8750 Å using the `scipy.curve_fit` routine, and the abundances from the best-fit spectra are adopted as the final measurements. During the fitting, the line-of-sight velocity ( $V_{\text{LOS}}$ ) is estimated simultaneously by the Doppler shift equation, with initial  $V_{\text{LOS}}$  set to the values from N23. We show two examples of the spectral fitting in the right panels of Fig. 1, where the observed MUSE spectra are compared with the DD-PAYNE best-fit for a P1 star (AO mode) and a P2 star (non-AO mode). In total, DD-PAYNE provides  $T_{\text{eff}}$ ,  $\log g$ , and 16 chemical abundances. Here we only focus on  $[\text{C}/\text{Fe}]$ ,  $[\text{N}/\text{Fe}]$ ,  $[\text{O}/\text{Fe}]$ ,  $[\text{Na}/\text{Fe}]$ ,  $[\text{Mg}/\text{Fe}]$ ,  $[\text{Ca}/\text{Fe}]$ , and  $[\text{Ba}/\text{Fe}]$ , which are well-known elements that show correlations or variations in different populations of globular clusters (e.g., C. I. Johnson & C. A. Pilachowski 2010; R. G. Gratton et al. 2012; N. Bastian & C. Lardo 2018). Z. Wang et al. (2022) reported typical precisions better than 0.2 dex for these elements from MUSE (see their Section 4 for details). It is worth noting that although DD-PAYNE provides  $[\text{Al}/\text{Fe}]$ , the associated uncertainty is large because most Al features lie outside the MUSE wavelength range (see Fig. 22 of X19). Therefore, we do not analyze  $[\text{Al}/\text{Fe}]$  from DD-PAYNE in this study. However, we include  $[\text{Ba}/\text{Fe}]$  because several strong absorptions can be detected by DD-PAYNE (see details in Section 3.1), and that X19 found it can be reasonably measured down to  $[\text{Fe}/\text{H}] = -4$  dex. This *s*-process element can also provide useful clues on the formation history of  $\omega$  Cen (e.g., A. F. Marino et al. 2011).

DD-PAYNE has two neural network models, DD-PAYNE-A (APOGEE-based) and DD-PAYNE-G (GALAH-based), and both can provide reliable abundance measurements. Although X19 provided recommendations for each element based on their validation

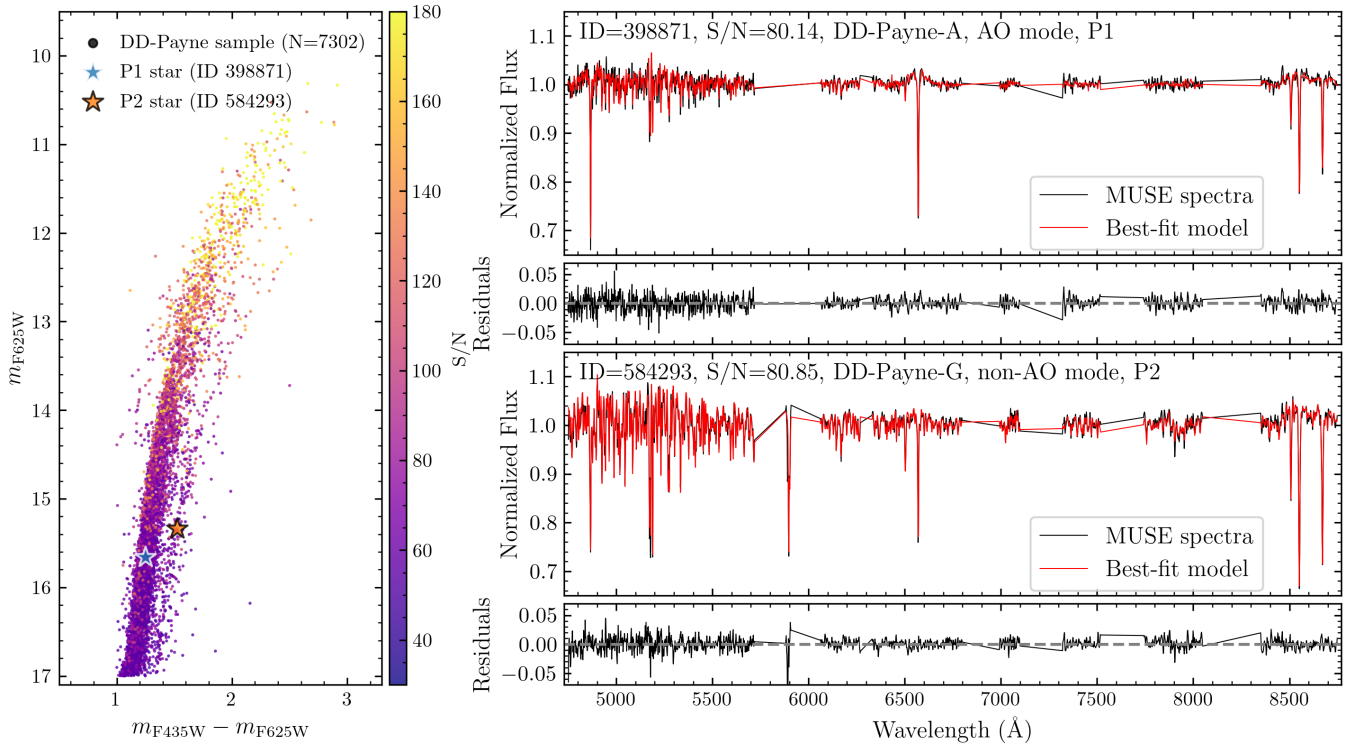


**Figure 1.** **Left:** Colour-magnitude diagram (CMD) of the oMEGACat DD-PAYNE sample using photometry from J. Anderson & R. P. van der Marel (2010), with stars color-coded by the MUSE spectral signal-to-noise ratio (S/N). The two stars shown in the right-hand panels are highlighted as filled star markers. **Right:** Example DD-PAYNE spectral fits for two stars. We show a primordial (P1) star and a chemically enhanced (P2) star (as defined in Section 5.1), fitted with the DD-PAYNE-A and DD-PAYNE-G models in AO and non-AO observations, respectively. Note that all stars, in both observing modes, are fitted with all DD-PAYNE models; the cases shown here are representative examples of the fitting performance.

tests, we preferentially adopt DD-PAYNE-A where available and use DD-PAYNE-G for abundances not provided by DD-PAYNE-A (notably [Na/Fe] and [Ba/Fe]). This is because almost all of our  $\omega$  Cen stars have metallicity lower than  $-0.5$  dex, while the DD-PAYNE-G has primarily training stars above  $[\text{Fe}/\text{H}] > -0.8$  dex. Fig. 6 of X19 shows that DD-PAYNE-G becomes more uncertain in  $T_{\text{eff}}$ ,  $\log g$ , and  $[\text{Fe}/\text{H}]$  at low metallicity, while DD-PAYNE-A remains robust down to  $[\text{Fe}/\text{H}] \approx -1.5$  dex. Therefore, we adopt  $T_{\text{eff}}$ ,  $\log g$ ,  $[\text{Fe}/\text{H}]$ ,  $[\text{C}/\text{Fe}]$ ,  $[\text{N}/\text{Fe}]$ ,  $[\text{O}/\text{Fe}]$ ,  $[\text{Mg}/\text{Fe}]$ ,  $[\text{Ca}/\text{Fe}]$  from DD-PAYNE-A and  $[\text{Na}/\text{Fe}]$  and  $[\text{Ba}/\text{Fe}]$  from DD-PAYNE-G, and we refer to Section 3 for detailed validation of the robustness of our abundance measurements.

From the MUSE spectra of 7,346 oMEGACat RGB stars, we apply the following selection criteria to select stars with good DD-PAYNE fitting:

$$\begin{cases} \text{red-}\chi_{\text{DD-PAYNE-A}}^2 < 20 \\ \text{red-}\chi_{\text{DD-PAYNE-G}}^2 < 20 \\ [\text{Fe}/\text{H}] > -2.394 \text{ dex,} \end{cases} \quad (2)$$

where  $\text{red-}\chi_{\text{DD-PAYNE-A}}^2$  and  $\text{red-}\chi_{\text{DD-PAYNE-G}}^2$  are the reduced chi-square values from the DD-PAYNE spectral

fitting. These thresholds were used to remove stars with poorly fitted spectra. The metallicity cut (using the uncalibrated  $[\text{Fe}/\text{H}]$ ) at  $-2.394$  dex excludes stars whose inferred metallicities lie at the edge of the model’s fitting range, where the DD-PAYNE measurements become unreliable. After applying these criteria, 7,302 stars remain in the sample, which we refer to as the oMEGACat DD-PAYNE catalog.

### 3. VALIDATION OF DD-PAYNE CHEMICAL ABUNDANCES

Before proceeding to the scientific analysis, we validate the chemical abundances derived with DD-PAYNE. We first examine whether DD-PAYNE correctly identifies the relevant spectral features for each element, particularly in the low-metallicity regime. We then directly compare the inferred abundances with high-resolution spectroscopic measurements from the literature using cross-matched samples. Finally, we calibrate the DD-PAYNE abundances onto a consistent literature scale to mitigate systematic offsets.

**Table 1.** Pearson correlation coefficients ( $r$ ) between DD-PAYNE gradient spectra (from X19) and Kurucz models in the LAMOST spectral resolution ( $R \sim 1800$ ) and MUSE fitting wavelength range (4750-8750 Å) at three metallicities ( $[\text{Fe}/\text{H}] = -2.5, -1.5, \text{ and } -0.5$  dex).

Parameter	$[\text{Fe}/\text{H}] = -2.5$	$[\text{Fe}/\text{H}] = -1.5$	$[\text{Fe}/\text{H}] = -0.5$
$T_{\text{eff}}^a$	0.768	0.806	0.785
$\log g^a$	0.426	0.568	0.656
$[\text{Fe}/\text{H}]^a$	0.866	0.896	0.849
$[\text{C}/\text{Fe}]^a$	0.124	0.207	0.782
$[\text{N}/\text{Fe}]^a$	0.018	0.117	0.681
$[\text{O}/\text{Fe}]^a$	0.021	0.056	0.621
$[\text{Na}/\text{Fe}]^b$	0.987	0.996	0.997
$[\text{Mg}/\text{Fe}]^a$	0.209	0.476	0.716
$[\text{Ca}/\text{Fe}]^a$	0.701	0.746	0.736
$[\text{Ba}/\text{Fe}]^b$	0.896	0.941	0.989

NOTE— (a) Gradient spectra from DD-PAYNE-A; (b) Gradient spectra from DD-PAYNE-G.

### 3.1. Measurement Robustness of DD-PAYNE

As noted by X19, the key factor enabling DD-PAYNE to recover chemical abundances reliably is the regularization of its training process by *ab initio* Kurucz spectral models (R. L. Kurucz 1970; R. Kurucz 1993; R. L. Kurucz 2005). During the training, DD-PAYNE calculates the correlation coefficients ( $r$ ) between its own gradient spectra and those from Kurucz models. The gradient spectrum is defined as  $\delta f_l / \delta l$ , where  $l$  is the stellar parameter and  $f_l$  is the predicted flux. These gradients reflect how the flux changes with each parameter, allowing the model to be constrained toward physically meaningful spectral responses even when the training set is limited. High correlations ( $r \geq 0.5$ ) indicate that DD-PAYNE can accurately identify the absorption features of each element, and low correlations ( $r < 0.5$ ) indicate that the abundance measurements from DD-PAYNE are purely from astrophysical correlations of the training sets. Therefore, before analyzing the  $\omega$  Cen MUSE spectral abundances, it is essential to confirm whether DD-PAYNE correctly identifies their spectral features.

To do this, we take three of the 16 sets of Kurucz gradient spectra calculated by X19 (see details in their Table 1) with  $[\text{Fe}/\text{H}]$  of  $-2.5, -1.5$  and  $-0.5$ , scaled-solar abundance ratios ( $[\text{X}/\text{Fe}]=0$ ), and  $\log g < 2.5$  dex. We choose these three sets because their  $[\text{Fe}/\text{H}]$  and  $\log g$  are the closest available matches to our  $\omega$  Cen RGB stars. We then compute the Pearson correlation coefficients ( $r$ ) between these Kurucz gradient spectra and those predicted by DD-PAYNE with the same stellar parameters.

The results are listed in Table 1. Overall, the correlations show the expected metallicity dependence, where the ability of DD-PAYNE to recover abundances declines as spectral features weaken at lower metallicities. For  $T_{\text{eff}}$ ,  $\log g$ , and  $[\text{Fe}/\text{H}]$ , the coefficients are high across all metallicities, confirming that they can be reliably measured. For  $[\text{C}/\text{Fe}]$ ,  $[\text{N}/\text{Fe}]$ , and  $[\text{O}/\text{Fe}]$ , the correlations are low at  $[\text{Fe}/\text{H}] = -2.5$  and  $-1.5$  dex, and the values become larger than 0.5 only at  $[\text{Fe}/\text{H}] = -0.5$  dex. This indicates that at very low metallicity, the relevant features become too weak for DD-PAYNE to identify. The  $[\text{Mg}/\text{Fe}]$  coefficients increase with metallicity, and the value becomes  $\sim 0.5$  when  $[\text{Fe}/\text{H}] > -1.5$  dex. The  $[\text{Ca}/\text{Fe}]$  coefficients are higher than 0.5 for all three metallicities, mostly due to the CaT absorptions (also shown in Fig. 1). For the abundances derived from the GALAH-based model (DD-PAYNE-G), both  $[\text{Na}/\text{Fe}]$  and  $[\text{Ba}/\text{Fe}]$  show correlation coefficients close to 1 at all metallicities. This indicates spectral features of these two abundances can be correctly identified. However, we note that most stars in the DD-PAYNE-G training set have  $[\text{Fe}/\text{H}] > -0.8$  dex. Therefore, these high correlations at low metallicity are primarily driven by the Kurucz model regularization rather than the training set data. In this regime, the  $[\text{Na}/\text{Fe}]$  and  $[\text{Ba}/\text{Fe}]$  abundances are extrapolated from higher-metallicity training data, but they remain physically constrained by the model regularization.

Based on these correlations, in this study, we adopt DD-PAYNE-A measurements of  $T_{\text{eff}}$ ,  $\log g$ ,  $[\text{Fe}/\text{H}]$ , and  $[\text{Ca}/\text{Fe}]$  at all metallicities,  $[\text{C}/\text{Fe}]$ ,  $[\text{N}/\text{Fe}]$ , and  $[\text{O}/\text{Fe}]$  for  $[\text{Fe}/\text{H}] > -1.0$  dex, and  $[\text{Mg}/\text{Fe}]$  for  $[\text{Fe}/\text{H}] > -1.5$  dex. For  $[\text{Na}/\text{Fe}]$  and  $[\text{Ba}/\text{Fe}]$ , we use the DD-PAYNE-G measurements across the full metallicity range. In Section 3.2, we examine the abundance measurement uncertainties through direct comparisons with high-resolution observations from the literature.

### 3.2. Comparing DD-PAYNE Abundances to Literature using Cross-matched Samples

To further test the accuracy of our DD-PAYNE abundances, in this section, we directly compare our abundance measurements with literature results derived from high-resolution spectroscopic observations of  $\omega$  Cen. This comparison provides a direct validation of both the absolute abundance scale and the abundance trends recovered from MUSE spectra.

#### 3.2.1. Cross-matching with Literature

We select five literature works that each have several hundred high-resolution spectroscopic observations of RGB stars in  $\omega$  Cen. The characteristics of these studies are summarized below:

**Table 2.** Residual statistics in the cross-matched sample between the oMEGACat DD-PAYNE catalog and literature datasets. For each quantity we list the number of matched stars ( $N$ ), mean residual  $\mu(\Delta)$ , and scatter  $\sigma(\Delta)$ , where  $\Delta X \equiv X_{\text{DD-PAYNE}} - X_{\text{lit}}$ .

Quantity	Johnson10+			Marino11/12+			Mészáros21+			AlvarezGaray22/24+			Schiavon24+		
	$N$	$\mu(\Delta)$	$\sigma(\Delta)$	$N$	$\mu(\Delta)$	$\sigma(\Delta)$	$N$	$\mu(\Delta)$	$\sigma(\Delta)$	$N$	$\mu(\Delta)$	$\sigma(\Delta)$	$N$	$\mu(\Delta)$	$\sigma(\Delta)$
$T_{\text{eff}}$ (K)	378	-96.20	66.88	172	293.65	93.46	66	69.68	113.46	223	100.56	130.22	195	129.83	95.34
$\log g$	378	0.61	0.22	172	0.42	0.24	66	0.27	0.26	223	0.36	0.23	195	0.39	0.23
[Fe/H]	378	0.32	0.12	172	0.36	0.11	66	0.11	0.13	223	0.31	0.09	195	0.23	0.07
[C/Fe]	0	...	...	70	0.37	0.46	33	-0.14	0.51	0	...	...	195	0.16	0.21
[N/Fe]	0	...	...	70	-0.40	0.43	12	-0.53	0.35	0	...	...	195	-0.39	0.31
[O/Fe]	376	0.33	0.29	153	0.16	0.38	23	-0.20	0.25	0	...	...	194	0.33	0.41
[Na/Fe]	299	0.23	0.28	142	0.18	0.29	3	0.36	0.18	148	0.31	0.26	143	0.30	0.52
[Mg/Fe]	0	...	...	0	...	...	60	-0.13	0.15	186	-0.09	0.18	195	0.05	0.15
[Ca/Fe]	378	-0.09	0.10	0	...	...	33	-0.13	0.15	0	...	...	191	-0.01	0.12
[Ba/Fe]	0	...	...	172	0.96	0.48	0	...	...	0	...	...	0	...	...

- [C. I. Johnson & C. A. Pilachowski \(2010\)](#): 855 RGB stars observed with Blanco/Hydra ( $R \sim 18,000$ ), providing abundances of Fe, O, Na, Al, Si, Ca, Sc, Ti, Ni, La, and Eu.
- [A. F. Marino et al. \(2011, 2012\)](#): 300 RGB stars observed with VLT/FLAMES ( $R \sim 20,000$ -25,000), measuring elements of Fe, Na, C, N, O, Ba, and La, where the C and N measurements are from [A. F. Marino et al. \(2012\)](#) for 77 stars.
- [S. Mészáros et al. \(2021\)](#): 982 RGB stars observed with APOGEE DR16 ( $R \sim 22,500$ ), including elements of Fe, C, N, O, Mg, Al, Si, K, Ca, and Ce measured using the BACCHUS code.
- [D. A. Alvarez Garay et al. \(2022, 2024\)](#): 450 RGB stars observed with VLT/FLAMES ( $R \sim 20,000$ -29,000), providing elements of Fe, Na, Mg, Al, Si, and K.
- [R. P. Schiavon et al. \(2024\)](#): 1,864 giant stars from APOGEE DR 17 with up to 20 elemental abundances measured from the ASPCAP pipeline.

We perform positional cross-matching between the oMEGACat DD-PAYNE catalog (obtained in Section 2.2) and each of these studies using right ascension ( $\alpha$ ) and declination ( $\delta$ ), and apply positional separation criteria to be less than 1 arcsec. The number of successfully matched stars with available abundances is listed in Table 2. Because our oMEGACat DD-PAYNE dataset focuses on  $\omega$  Cen central regions and most literature stars are at larger radii, only a small fraction of stars are cross-matched. Nevertheless, the cross-matched samples with more than 100 stars are sufficient for a direct comparison of their abundance measurements.

### 3.2.2. Comparing the Chemical Abundances

Fig. 2 presents one-to-one comparisons of our DD-PAYNE abundance measurements with literature values for the cross-matched stars. Each color corresponds to a literature study, and the point sizes correlate with  $S/N_{\text{MUSE}}$ . The black dashed lines indicate the one-to-one relation. Note that we do not show the formal uncertainties of each stellar parameter from the DD-PAYNE spectral fitting in Fig. 2 given studies have shown that they are underestimated ([Z. Wang et al. 2022](#); [N. R. Sandford et al. 2020](#)). Instead, we use their deviations from literature measurements as an indicator of the measurement uncertainties. As shown in Fig. 2,  $T_{\text{eff}}$ ,  $\log g$ , and [Fe/H] show strong correlations with literature values but with a constant offset. This confirms that DD-PAYNE provides reliable measurements of  $T_{\text{eff}}$ ,  $\log g$ , and [Fe/H] from MUSE spectra. For [C/Fe] and [N/Fe], the literature measurements span a wider abundance range, while the DD-PAYNE results show narrower distributions. [O/Fe] and [Na/Fe] demonstrate larger scatters than  $T_{\text{eff}}$ ,  $\log g$ , and [Fe/H]. The [Mg/Fe] comparison shows two sequences, which is likely because the DD-PAYNE-A training set is dominated by Milky Way field stars and the model tends to reproduce the  $\alpha$ -bimodality of the Galactic disk (e.g., [M. R. Hayden et al. 2015](#)). However, the literature measurements also exhibit a similar but less pronounced bimodal feature (see discussions in Section 4.2), indicating that this structure might not be solely driven by the training data. We will assess the impact on Mg measurements in detail in Section 4.2 and 5.1. Another  $\alpha$ -element [Ca/Fe] also shows a scattered distribution, but the ranges on both axes are narrower than for the other elements. The  $s$ -process element [Ba/Fe] shows a constant offset, with significant scatter

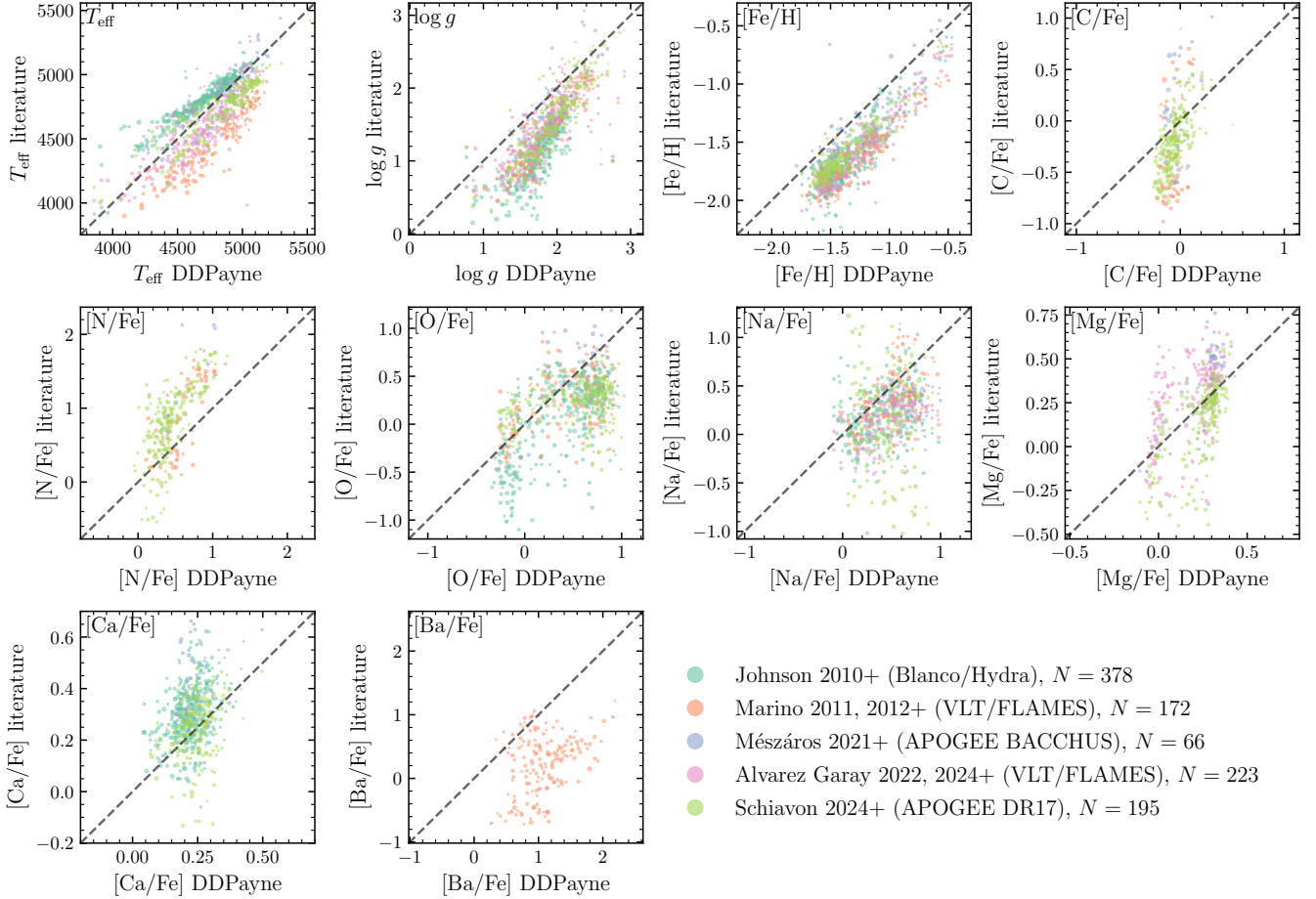


**Figure 2.** Direct comparison of DD-PAYNE abundance measurements for oMEGACat DD-PAYNE stars with literature values for the cross-matched samples. Common stars between oMEGACat and each literature catalog are shown in different colors, with point size indicating  $S/N_{\text{MUSE}}$ . The number of common stars is provided in the legend for each literature work, and the black dashed lines are the one-to-one relation for visual reference.

at  $[\text{Ba}/\text{Fe}] \sim 1$  dex. This figure quantitatively demonstrates the difference in chemical abundances measured from DD-PAYNE and high-resolution spectroscopic observations in the literature.

Although Fig. 2 shows scatters in the direct abundance comparison between DD-PAYNE and literature, one thing to note is that the literature measurements are not the “true” answers as they also have measurement errors. To further quantify the abundance differences, we plot in Fig. 3 the median and standard deviation of the DD-PAYNE abundance difference relative to the literature measurements, with the values also shown in Table 2. We also plot in gray the median and dispersion between different literature studies themselves using their cross-matched stars for comparison. As Fig. 3 shows, the abundance difference between literature studies is often comparable to that between DD-PAYNE and literature. Notably,  $[\text{Na}/\text{Fe}]$  from (R. P. Schiavon et al. 2024) (bottom panel) shows a much

larger scatter than the other elements due to the highly uncertain Na measurements from APOGEE spectra, as discussed in M. Shetrone et al. (2026). Overall, this figure implies that DD-PAYNE-inferred abundance uncertainties are of the same order as inter-study systematics in high-resolution spectroscopic observations. Therefore, although DD-PAYNE does not reach the abundance precision of high-resolution spectroscopy for individual stars, given the larger sample, its measurements are sufficiently robust for statistical analyses of abundance relations. Once the DD-PAYNE-inferred abundances are calibrated to the high-resolution scale, the dataset can be combined with existing literature to significantly expand the abundance sample of  $\omega$  Cen, particularly within its half-light radius and in the relatively metal-rich regime ( $[\text{Fe}/\text{H}] > -1$  dex). This enables a more comprehensive characterization of  $\omega$  Cen’s chemical abundance patterns and its enrichment history.

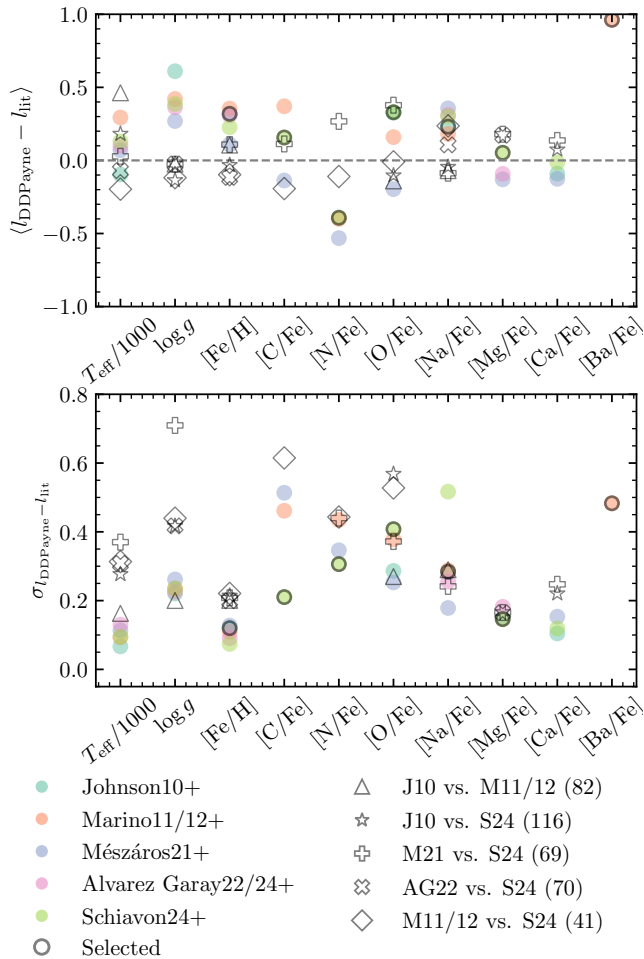


**Figure 3.** Median (top panel) and standard deviation (bottom panel) of the differences between oMEGACat DD-PAYNE abundances and literature studies for the cross-matched stars. The color scheme for each literature is the same as in Fig. 2. Gray markers with different shapes indicate comparisons of cross-matched stars between different literature, with the number of stars shown in parentheses. The open circle marker labeled “Selected” indicates the reference literature used for the abundance calibration of each element. As discussed in detail in Section 3.3, we adopt  $[\text{Fe}/\text{H}]$ , and  $[\text{Na}/\text{Fe}]$  from C. I. Johnson & C. A. Pilachowski (2010);  $[\text{C}/\text{Fe}]$ ,  $[\text{O}/\text{Fe}]$ ,  $[\text{N}/\text{Fe}]$ , and  $[\text{Mg}/\text{Fe}]$  from R. P. Schiavon et al. (2024); and  $[\text{Ba}/\text{Fe}]$  from A. F. Marino et al. (2011) as references to calibrate DD-PAYNE abundances.

### 3.3. Calibrating DD-PAYNE Abundances to the Literature Scale

To calibrate DD-PAYNE abundances to the literature scale, we first determine which literature to adopt as the “standard” reference for each element. The selected references are marked with gray circles in Fig. 3. Specifically, we adopt  $[\text{Fe}/\text{H}]$ , and  $[\text{Na}/\text{Fe}]$  from C. I. Johnson & C. A. Pilachowski (2010);  $[\text{C}/\text{Fe}]$ ,  $[\text{O}/\text{Fe}]$ ,  $[\text{N}/\text{Fe}]$ , and  $[\text{Mg}/\text{Fe}]$  from R. P. Schiavon et al. (2024); and  $[\text{Ba}/\text{Fe}]$

from A. F. Marino et al. (2011). These choices are either due to the smallest standard deviation of abundance differences relative to DD-PAYNE (bottom panel of Fig. 3) or the largest number of cross-matched stars, as summarized in Table 2. Notably, we adopt  $[\text{C}/\text{Fe}]$ ,  $[\text{N}/\text{Fe}]$ , and  $[\text{O}/\text{Fe}]$  from the same literature to avoid systematic biases from different measurement methods, which is essential for investigating the  $[(\text{C}+\text{N}+\text{O})/\text{Fe}]$  distribution later in this study. As for  $[\text{Ca}/\text{Fe}]$ , we do not perform an abundance calibration because it shows the smallest deviation ( $\sigma(\Delta) \sim 0.1$  dex) compared to other parameters.

We then use these reference datasets to calibrate the DD-PAYNE abundance measurements. First, we plot the abundance differences ( $\Delta[\text{X}/\text{Fe}]$ ) between DD-PAYNE and the reference literature as a function of metallicity, as shown in Fig. 4. For each element, we show only the comparison with the selected reference study, using the same color scheme as in Fig. 2. We divide the stars into nine  $[\text{Fe}/\text{H}]$  bins and calculate the median and 16th-84th percentile values (black points with error bars) to evaluate how the offsets vary with metallicity. As shown in Fig. 4,  $[\text{Fe}/\text{H}]$  shows nearly constant offsets, whereas other elements show larger median offsets and scatter at lower metallicities. This behavior is expected because the DD-PAYNE training set includes fewer stars with  $[\text{Fe}/\text{H}] < -1$  dex. In particular,  $\Delta[\text{Ba}/\text{Fe}]$  shows a clear transition near  $[\text{Fe}/\text{H}] \sim -1$  dex, changing from positive values in the metal-poor regime to values near zero at higher metallicity. This explains the  $[\text{Ba}/\text{Fe}]$  behavior we see in Fig. 2, where the stars align closest to the one-to-one relation should be mostly metal-rich. Although we do not apply a calibration to  $[\text{Ca}/\text{Fe}]$ , we still compare it with C. I. Johnson & C. A. Pilachowski (2010) in Fig. 4 as a showcase of DD-PAYNE reliability. The resulting  $\mu$  and  $\sigma$  values show that it is highly consistent with literature.

To correct these systematic offsets, we apply a metallicity-dependent calibration using the  $\Delta[\text{X}/\text{Fe}]$ -metallicity relations shown in Fig. 4. For each element, we fit a second-degree polynomial to model the offset as a function of  $[\text{Fe}/\text{H}]$  (originally from DD-PAYNE without calibration), and then add this calibration term ( $\Delta[\text{X}/\text{Fe}]$ ) to the original DD-PAYNE abundances. The fitted polynomial relations are shown as black dashed lines in Fig. 4. In the following analysis, all abundance measurements are based on these calibrated values, except for  $[\text{Ca}/\text{Fe}]$ , unless otherwise noted. For metallicity, we use  $[\text{Fe}/\text{H}]_{\text{uncal}}$  to denote the original DD-PAYNE metallicity measurement, and  $[\text{Fe}/\text{H}]$  to denote the calibrated metallicity.

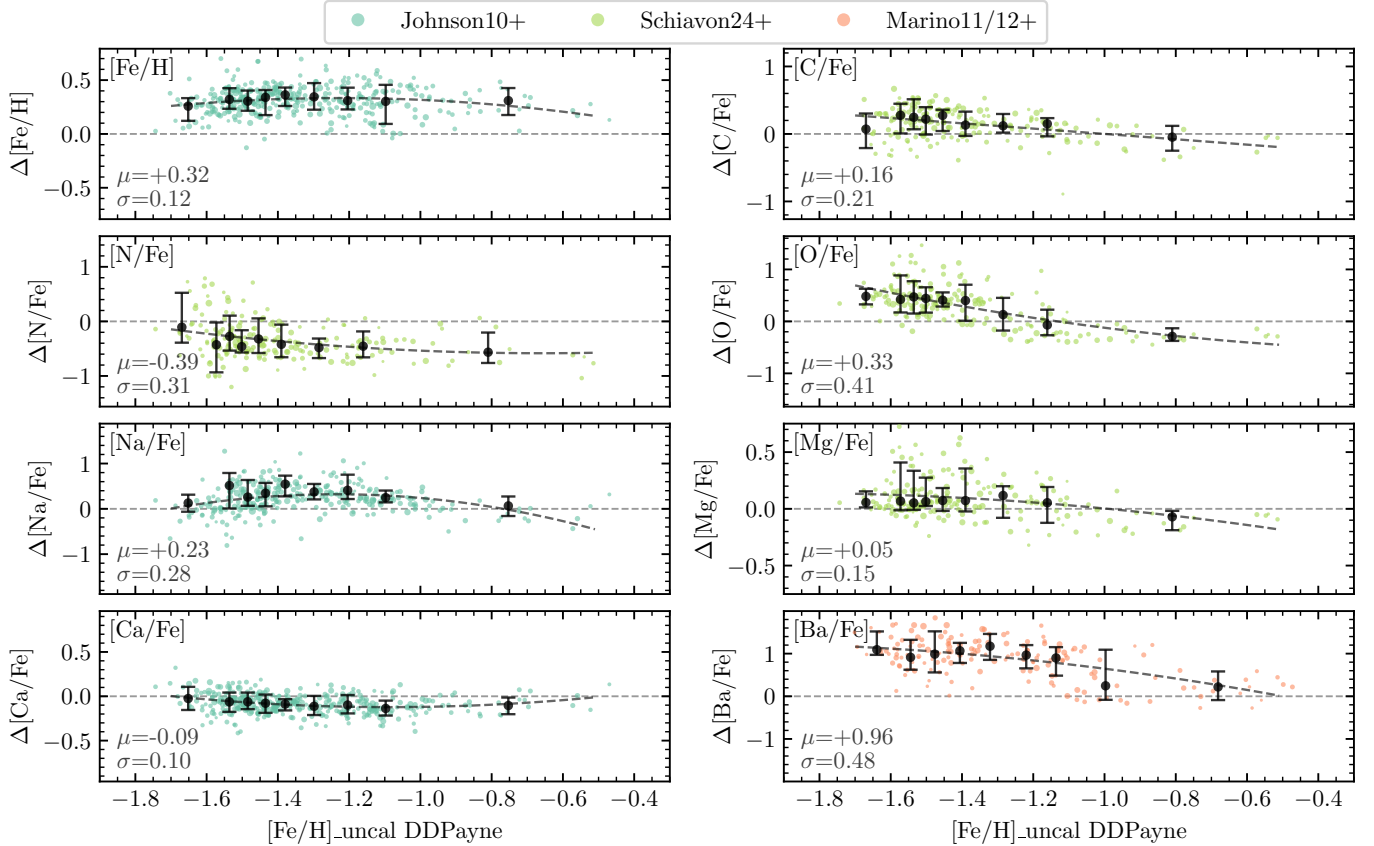


**Figure 4.** Difference between oMEGACat DD-PAYNE abundances and literature measurements ( $\Delta[X/\text{Fe}]$ ) as a function of  $[\text{Fe}/\text{H}]$  (original DD-PAYNE measurements without calibration). For each element, we use the standard reference literature adopted in Section 3.3. The stars are divided into nine  $[\text{Fe}/\text{H}]$  bins, and the median  $\Delta[X/\text{Fe}]$  values are plotted as black points with error bars represented by the 16<sup>th</sup> and 84<sup>th</sup> percentiles. The gray dashed lines represent the fitted second-degree polynomial relations used to calibrate the DD-PAYNE abundances to the literature scale, as described in Section 3.3. In each panel, the annotation in the lower-left corner reports the overall median  $\Delta[X/\text{Fe}]$  and  $\sigma \equiv (p_{84} - p_{16})/2$  computed from all stars shown in that panel; these values are also listed in Table 2.

## 4. RESULTS

### 4.1. Abundance Quality Selection of oMEGACat DD-PAYNE Catalog

Based on the reliability assessment of the DD-PAYNE measurements in Section 3.1, we use  $[\text{C}/\text{Fe}]$ ,  $[\text{N}/\text{Fe}]$ , and  $[\text{O}/\text{Fe}]$  only for stars with  $[\text{Fe}/\text{H}]_{\text{uncal}} > -1.0$  dex and  $m_{\text{F625W}} > 14$  mag (505 stars), where the magnitude cut-off is applied to remove the effect of CNO variations above the RGB bump in the subsequent analysis (e.g., C. Lardo et al. 2012). For  $[\text{Mg}/\text{Fe}]$ , we only use stars with  $[\text{Fe}/\text{H}]_{\text{uncal}} > -1.5$  dex (3,563 stars). For  $T_{\text{eff}}$ ,  $\log g$ ,  $[\text{Fe}/\text{H}]$ ,  $[\text{Na}/\text{Fe}]$ ,  $[\text{Ca}/\text{Fe}]$ , and  $[\text{Ba}/\text{Fe}]$ , we include all stars across the full metallicity range (7,302 stars). Additionally, because  $[\text{Na}/\text{Fe}]$  is primarily constrained by the Na I D region (X19), we use only stars observed in non-adaptive-optics (non-AO) mode when analyzing  $[\text{Na}/\text{Fe}]$  (5,881 stars). In AO-mode observations, the Na I D is masked to block laser contamination, leading to unreliable  $[\text{Na}/\text{Fe}]$  measurements. We publish our final

oMEGACat DD-PAYNE catalog as an online machine-readable table, including  $\text{S}/\text{N}_{\text{MUSE}}$ ,  $T_{\text{eff}}$ ,  $\log g$ ,  $[\text{Fe}/\text{H}]$ , individual abundance measurements, and literature star identifiers. The column descriptions are provided in Table 3. We note that the table also includes the formal uncertainties of the individual stellar measurements (re-calculated due to the abundance calibration described in Section 3.3) for reference, although these uncertainties are underestimated.

### 4.2. Chemical Abundance Patterns with Metallicity

Fig. 5 shows the DD-PAYNE chemical abundances as a function of  $[\text{Fe}/\text{H}]$  (contours and gray points) for  $[\text{Na}/\text{Fe}]$ ,  $[\text{Mg}/\text{Fe}]$ ,  $[\text{Ca}/\text{Fe}]$ , and  $[\text{Ba}/\text{Fe}]$ , with literature measurements shown as colored points. We focus on these three elements because Section 3.1 demonstrated that the spectral features can be correctly identified in a relatively wide metallicity range. For literature data, we show only the studies adopted for the metallicity-

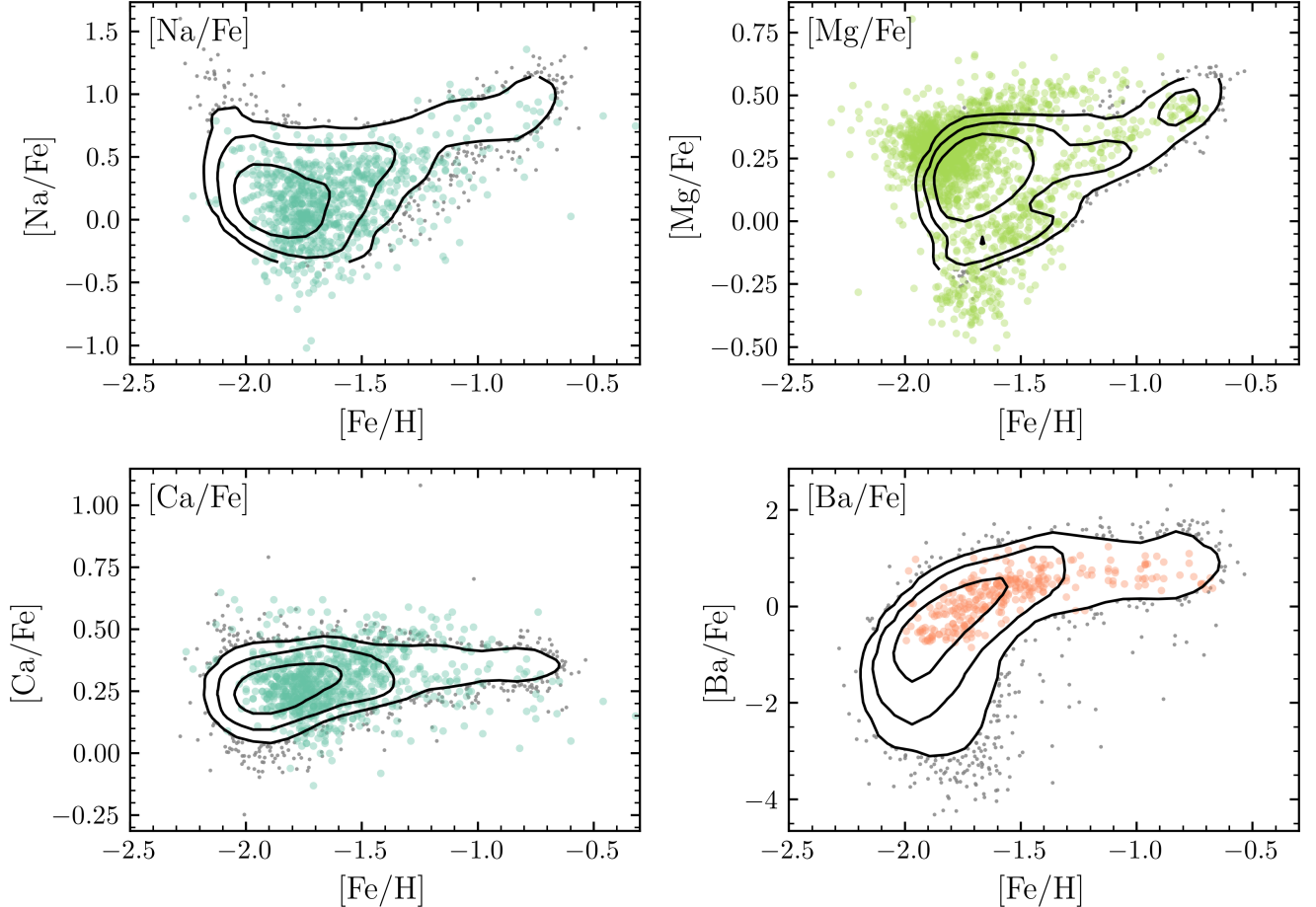


**Figure 5.** Chemical abundances of  $\omega$  Cen stars as a function of  $[\text{Fe}/\text{H}]$ . The DD-PAYNE measurements are shown as black density contours (50%, 80%, and 95% enclosed probability), while only the lowest-density of stars are over-plotted in gray to show the outer envelope. Colored points show literature measurements used as calibration references in Section 3.3, using the same color scheme as Fig. 2. For the  $[\text{Mg}/\text{Fe}]-[\text{Fe}/\text{H}]$  relation, only stars with DD-PAYNE  $[\text{Fe}/\text{H}]_{\text{uncal}} > -1.5$  dex are shown.

dependent calibration in Section 3.3 with the same color scheme as Fig. 2.

As shown in Fig. 5, the calibrated DD-PAYNE abundance-metallicity relations for  $[\text{Na}/\text{Fe}]$ ,  $[\text{Mg}/\text{Fe}]$ , and  $[\text{Ba}/\text{Fe}]$  agree well with the literature trends, and the original DD-PAYNE measurements of  $[\text{Ca}/\text{Fe}]$  are also consistent with the literature.  $[\text{Na}/\text{Fe}]$  increases with metallicity, and its dispersion is consistent with the high-resolution measurements of C. I. Johnson & C. A. Pilachowski (2010).  $[\text{Mg}/\text{Fe}]$  exhibits more complex structure in the DD-PAYNE data, while the literature measurements (R. P. Schiavon et al. 2024) show two distinct sequences; both datasets display an overall increasing trend with  $[\text{Fe}/\text{H}]$ . The two sequences in literature correspond to the primordial-Mg and Mg-depleted stars associated with the Mg-Al cycle, where Mg is converted into Al only in high-temperature environments ( $T \simeq 10^7$  K; e.g., D. A. Alvarez Garay et al. 2024; A. C.

Mason et al. 2025). Compared to the literature, the DD-PAYNE results partially reveal the two sequences, although they appear to merge at intermediate metallicity ( $[\text{Fe}/\text{H}] \sim -1.2$  dex). This could be due to the lack of stars with  $[\text{Fe}/\text{H}]_{\text{uncal}} < -1.5$  dex in this panel, which affects the contour determination. It also likely reflects the larger  $[\text{Mg}/\text{Fe}]$  uncertainties in the DD-PAYNE estimates and the influence of Milky Way field stars that dominate the DD-PAYNE training set. The  $s$ -process element  $[\text{Ba}/\text{Fe}]$  increases continuously with metallicity, reaching super-solar values near  $[\text{Fe}/\text{H}] = -1.5$  dex, which is also observed in A. F. Marino et al. (2011). Compared to the A. F. Marino et al. (2011) data, DD-PAYNE yields  $[\text{Ba}/\text{Fe}]$  values as low as  $-2.0$  dex for the most metal-poor stars. In conclusion, after applying the metallicity-dependent calibration, the DD-PAYNE abundances reproduce the overall abundance-metallicity trends reported in previous literature studies.

**Table 3.** Column descriptions of the oMEGACat DD-PAYNE catalog, published as an online machine-readable table.

Column	Description	Unit
R.A.	Right Ascension (J2000) from N23	deg
Decl.	Declination (J2000) from N23	deg
ID_MUSE	oMEGACat MUSE catalog identifier from N23	
ID_J10	Identifier from C. I. Johnson & C. A. Pilachowski (2010)	
ID_M1112	Identifier from A. F. Marino et al. (2011, 2012)	
ID_M21	Identifier from S. Mészáros et al. (2021)	
ID_AG2224	Identifier from D. A. Alvarez Garay et al. (2022, 2024)	
ID_S24	Identifier from R. P. Schiavon et al. (2024)	
S/N	Average MUSE spectral signal-to-noise ratio on the full wavelength	pix <sup>-1</sup>
$T_{\text{eff}}$	Effective temperature from DD-PAYNE	K
$e_{T_{\text{eff}}}$	Formal uncertainty in $T_{\text{eff}}$	K
$\log g$	Surface gravity from DD-PAYNE	dex
$e_{\log g}$	Formal uncertainty in $\log g$	dex
[Fe/H]	Metallicity from DD-PAYNE	dex
$e_{\text{[Fe/H]}}$	Formal uncertainty in [Fe/H]	dex
[X/Fe]	Chemical abundance in [X/Fe] for C, N, O, Na, Mg, Ca, and Ba from DD-PAYNE	dex
$e_{\text{[X/Fe]}}$	Formal uncertainty of each chemical abundance in [X/Fe]	dex
$\chi_{\text{red,A}}^2$	Reduced- $\chi^2$ of the DD-PAYNE-A spectral fitting	
$\chi_{\text{red,G}}^2$	Reduced- $\chi^2$ of the DD-PAYNE-G spectral fitting	

NOTE— (1) Abundances are calibrated to the literature scale except for [Ca/Fe], as detailed in Section 3.3.

(2) Uncertainties are the formal (statistical) errors returned by the DD-PAYNE spectral fitting and are recalculated to include the abundance calibration described in Section 3.3 using uncertainty propagation equations. These uncertainties are however noted to be underestimated.

(3) [C/Fe], [N/Fe], and [O/Fe] are reported only for stars with  $[\text{Fe}/\text{H}]_{\text{uncal}} > -1.0$  dex.

(4) [Mg/Fe] is reported only for stars with  $[\text{Fe}/\text{H}]_{\text{uncal}} > -1.5$  dex.

(5) [Na/Fe] is reported only for stars observed in MUSE non-AO mode.

### 4.3. Chromosome Diagram with Chemical Abundances

Our oMEGACat spectra are located in the central regions of the cluster, and thus can be cross-correlated with multi-band HST photometry (H24) in much greater numbers than any previous high-resolution abundance measurements. We focus in this section on the chromosome (or pseudo color-color) diagram, which is a powerful tool for analyzing multiple stellar populations with their abundance variations in globular clusters. Its two

axes are constructed from specific photometric bands to trace abundance variations (e.g., L. Sbordone et al. 2011; A. P. Milone et al. 2017b). By combining the multi-band HST photometry from oMEGACat (H24) with our DD-PAYNE abundance measurements, we study the distribution of chemical abundances across the chromosome diagram. In Fig. 6, each panel shows the chromosome diagram color-coded by a DD-PAYNE-inferred abundance. The chromosome diagrams are plotted using the pseudo-colors ( $x$  and  $y$  coordinates) provided by C. Clontz et al. (2025b). We plot [Fe/H], [Na/Fe], [Ca/Fe], and [Ba/Fe] across the full metallicity range. [C/Fe], [N/Fe], and [O/Fe] are restricted to  $[\text{Fe}/\text{H}]_{\text{uncal}} > -1.0$  dex and [Mg/Fe] is restricted to  $[\text{Fe}/\text{H}]_{\text{uncal}} > -1.5$  dex. We also plot individual abundance measurements for C, N, and O from APOGEE DR17 (R. P. Schiavon et al. 2024) to show their values in the metal-poor regime. The black lines indicate the upper (P2), middle (Im), and lower (P1) stellar stream selections as defined by C. Clontz et al. (2025b).

As shown in Fig. 6, [Fe/H] shows a diagonal gradient in the chromosome diagram, and it has a correlation with the  $\Delta_{275,814}$  axis. This is consistent with results from M. S. Nitschai et al. (2024); M. Latour et al. (2025). Among the light elements, [C/Fe], [N/Fe], and [O/Fe] display clear abundance variations between the P1 and P2 streams in the metal-rich regime, although the P1 stream contains only a handful of stars at these metallicities. In the metal-poor regime, [N/Fe] and [O/Fe] measurements from APOGEE DR17 show smooth variations, while the behavior of [C/Fe] is unclear. [Na/Fe] and [Mg/Fe] exhibit both diagonal and vertical gradients, reflecting the abundance differences in different populations. Similar to [Fe/H], [Ca/Fe] shows a general increasing trend along the x-axis. Notably, [Ba/Fe] shows a transition near  $\Delta_{275,814} \sim 0$ , corresponding to the lowest-metallicity regime. This behavior primarily reflects the rapid increase of [Ba/Fe] with metallicity between  $[\text{Fe}/\text{H}] \sim -2.0$  and  $-1.5$  dex (see Fig. 5), after which the trend flattens.

Compared with traditional high-resolution spectroscopic studies that typically target hundreds of RGB stars, the oMEGACat DD-PAYNE dataset enables statistical analyses of abundance variations across the chromosome diagram for Fe, Na, Mg, Ca, and Ba, where the sample size is much larger. For C, N, and O, the measurements in the metal-rich regime provide a valuable complement to previous literature studies. The trends observed here are consistent with those found in high-resolution studies of individual stars (C. I. Johnson & C. A. Pilachowski 2010; A. F. Marino et al. 2011, 2012; R. P. Schiavon et al. 2024), demonstrating that

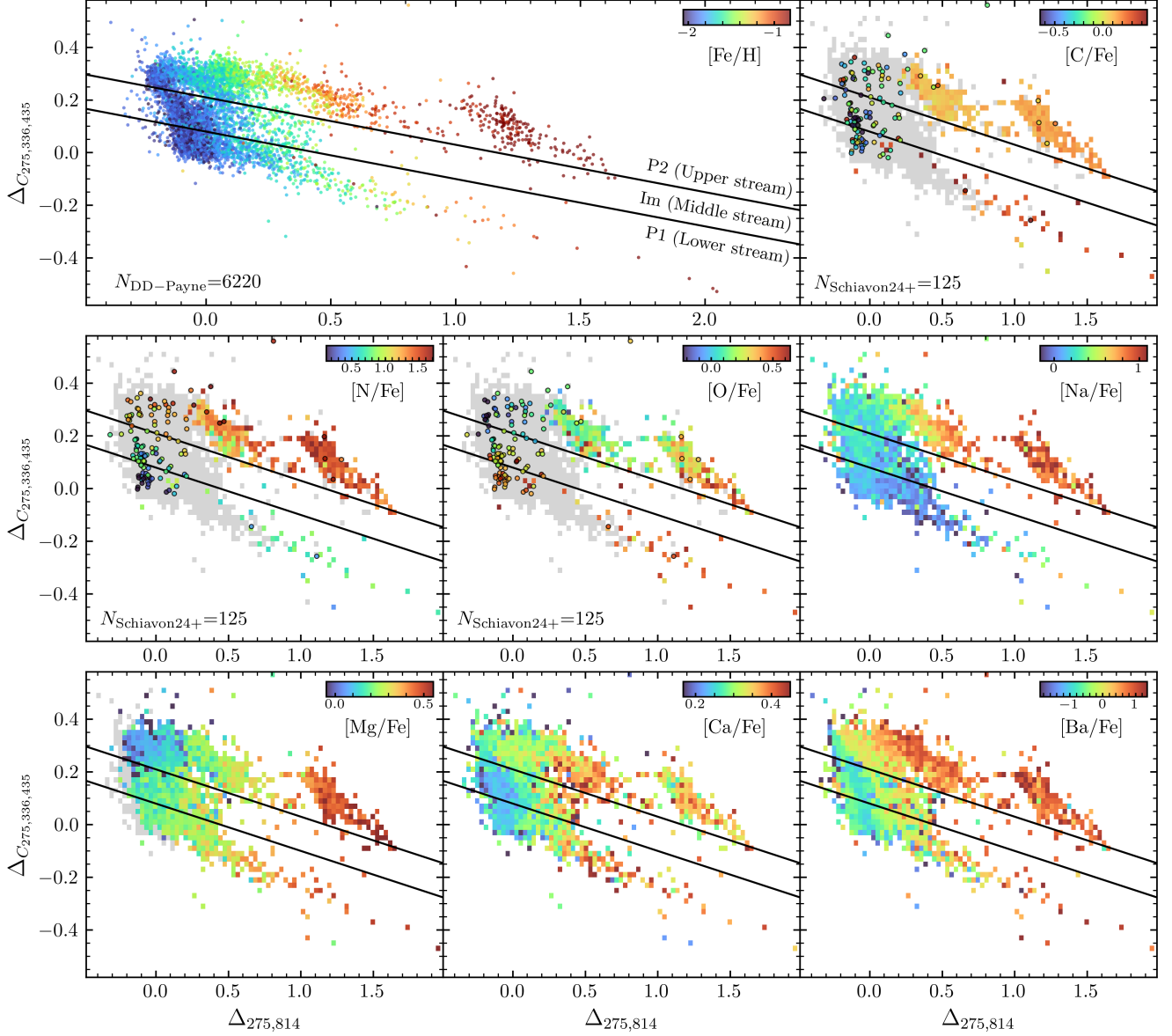


**Figure 6.** Chromosome diagram of  $\omega$  Cen stars. The top-left panel shows individual stars from the oMEGACat DD-PAYNE sample, color-coded by  $[\text{Fe}/\text{H}]$ . The remaining panels show the median DD-PAYNE chemical abundances calculated using stars within each grid cell (0.035 on the x-axis and 0.02 on the y-axis). Particularly, DD-PAYNE measurements of  $[\text{C}/\text{Fe}]$ ,  $[\text{N}/\text{Fe}]$ , and  $[\text{O}/\text{Fe}]$  are shown only for stars with  $[\text{Fe}/\text{H}]_{\text{uncal}} > -1$  dex, and  $[\text{Mg}/\text{Fe}]$  only for stars with  $[\text{Fe}/\text{H}]_{\text{uncal}} > -1.5$  dex. Gray regions in the  $[\text{C}/\text{Fe}]$ ,  $[\text{N}/\text{Fe}]$ ,  $[\text{O}/\text{Fe}]$ , and  $[\text{Mg}/\text{Fe}]$  panels are areas excluded by these cuts. We also plot individual abundance measurements for C, N, and O from APOGEE DR17 (R. P. Schiavon et al. 2024) to show their variance in the metal-poor regime. Black lines indicate the boundaries of the upper (P2), middle (Im), and lower (P1) stellar streams defined in C. Clontz et al. (2025b).

machine-learning-based abundance measurements from MUSE spectra can effectively reproduce key chemical features of  $\omega$  Cen’s multiple stellar populations.

## 5. DISCUSSION

### 5.1. Abundance Variations in P1, Im, and P2 Streams

As shown in Fig. 6, the distribution of stars on the chromosome diagram clearly reveals the presence of mul-

multiple stellar populations in  $\omega$  Cen. The most common classification divides stars into two primary groups, P1 and P2, which has been widely adopted to study abundance variations in globular clusters (e.g., A. F. Marino et al. 2011, 2012). Recent studies identified another “Intermediate” (Im) population having a narrower metallicity spread than P1 and P2 (A. F. Marino et al. 2019; C. Clontz et al. 2025b; A. C. Mason et al. 2025; E. Don-

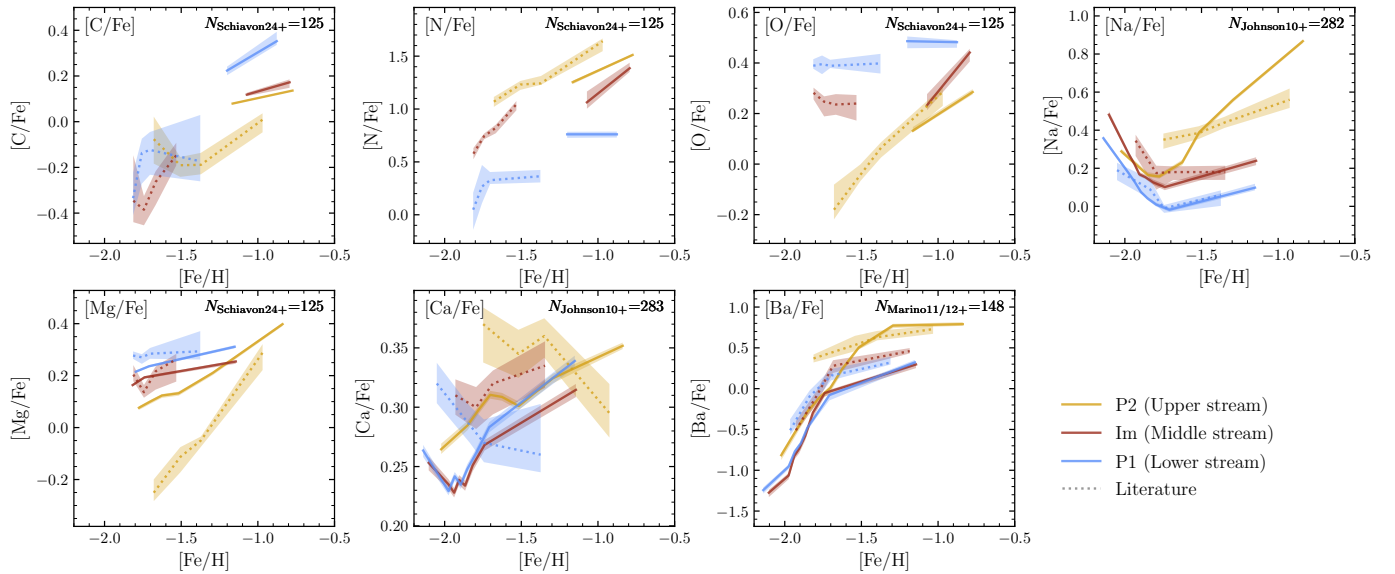


**Figure 7.** Chemical abundances as a function of  $[\text{Fe}/\text{H}]$ . Abundances for the three streams are noted as Upper (P2), Middle (Im), and Lower (P1), as defined by the black solid lines in Fig. 6. We plot the median trend for each stream, with shaded regions representing the standard error of the mean (SEM). All  $[\text{Fe}/\text{H}]$  bins are constructed separately for each stream and dataset to contain equal numbers of stars; the number per bin ranges from 7 to 332 depending on the element and sample size. Solid lines represent DD-PAYNE measurements (selected via criteria in Section 4.1). Dashed lines indicate literature results with the reference and number of stars written in the top right corner of each panel.

doglio et al. 2026) although the exact naming of these three different populations varies between these studies. C. Clontz et al. (2025b) compared the chromosome diagram with theoretical isochrones and demonstrated that the P2 population is helium-enhanced across all metallicities compared to P1 and Im ( $\Delta Y_{\min} \geq 0.11$ ). In this subsection, we adopt the classification of three primary populations from C. Clontz et al. (2025b), dividing our oMEGACat DD-PAYNE sample into Upper (P2), Middle (Intermediate), and Lower (P1) streams to investigate their chemical abundance distinctions.

The results are shown in Fig. 7, where we compare the median abundance trends with error bars calculated using the standard error of the mean (SEM; shaded regions) of the three streams using DD-PAYNE measurements (solid lines) based on the selection criteria in Section 4.1, together with literature data (dashed lines). For consistency, the literature datasets used for each element are the same as those adopted for the metallicity-dependent calibration in Section 3.3. The boundaries defining the three streams are indicated by the black lines in Fig. 6.

For C, N, and O, as shown in Fig. 7, our DD-PAYNE measurements extend the literature abundance-metallicity relations to higher metallicities. From the combined datasets,  $[\text{N}/\text{Fe}]$  shows a clear increase with metallicity for P2 and Im, whereas P1 is relatively flat with a mild overall increase. For  $[\text{O}/\text{Fe}]$ , P2 shows the strongest increase with metallicity, Im exhibits a weaker

increasing trend, and P1 is mostly constant. Both  $[\text{N}/\text{Fe}]$  and  $[\text{O}/\text{Fe}]$  show clear offsets between the three streams.  $[\text{N}/\text{Fe}]$  increases from P1, Im to P2, whereas  $[\text{O}/\text{Fe}]$  follows the opposite ordering, with P2 being the most O-depleted and P1 the most O-enhanced. This ordering illustrates the N-O anti-correlation across all metallicities. Consistent with A. F. Marino et al. (2012), we do not find a strong internal  $[\text{C}/\text{Fe}]$ -metallicity trend within any individual stream. The literature  $[\text{C}/\text{Fe}]$  measurements are highly scattered with large SEM, which is also seen in the chromosome diagram in Fig. 6. However, the overall  $[\text{C}/\text{Fe}]$  seems to increase with metallicity with the newly included DD-PAYNE measurements on the metal-rich end.

Furthermore,  $[\text{Na}/\text{Fe}]$  also shows distinct trends among the three streams: it decreases at the lowest metallicities and then increases toward higher  $[\text{Fe}/\text{H}]$ , with P2 being more Na-enriched than P1 and Im. The DD-PAYNE trend for P2 also appears to increase more steeply than in the literature.  $[\text{Mg}/\text{Fe}]$  is mildly increasing with metallicity in P1 and Im, while P2 is Mg-depleted but shows a steeper increase toward higher metallicities. Although P1 and Im show consistent trends between DD-PAYNE and the literature, the P2 stream in the literature extends to lower values ( $[\text{Mg}/\text{Fe}] \sim -0.2$  dex) than in the DD-PAYNE measurements. This discrepancy is likely caused by the DD-PAYNE training set, which is dominated by Milky Way field stars and therefore affects the abundance estimates

for the Mg-depleted stars. Both the DD-PAYNE and literature measurements of  $[\text{Ca}/\text{Fe}]$  lie within a similarly narrow range (0.23-0.39 dex), although the P2 population in the literature shows a decreasing trend with metallicity.

For the  $s$ -process element  $[\text{Ba}/\text{Fe}]$ , all three streams in Fig. 6 show an increasing trend with  $[\text{Fe}/\text{H}]$  which flattens toward the metal-rich end. Notably, despite small offsets between the DD-PAYNE (solid lines) and A. F. Marino et al. (2011) (dotted lines) measurements, both datasets show that P2 reaches a higher  $[\text{Ba}/\text{Fe}]$  value than P1 and Im. This feature was not detected by A. F. Marino et al. (2012), who found no significant difference in  $[\text{La}/\text{Fe}]$ —another heavy  $s$ -process element—between their P1 and P2 populations. However, using  $[\text{La}/\text{Fe}]$  from both A. F. Marino et al. (2012) and R. P. Schiavon et al. (2024), we find that P2 is indeed more enhanced than P1 and Im under our population definition, at a level comparable to  $[\text{Ba}/\text{Fe}]$ . Therefore, we believe that the enhanced  $s$ -process enrichment in P2 stars is a real signature, and the non-detection of A. F. Marino et al. (2012) is due to the different definitions of P1 and P2, as their classification is based on the Na-O anti-correlation. Ba enhancement in P2-like stars has also been reported in other globular clusters (e.g., N. Kacharov & A. Koch 2013; A. F. Marino et al. 2019). Our finding is further supported by recent studies of  $\omega$  Cen (A. C. Mason et al. 2025; E. Donoghio et al. 2026), who reported similar results using  $s$ -process elements  $[\text{Ce}/\text{Fe}]$ ,  $[\text{Ba}/\text{Fe}]$ , and  $[\text{La}/\text{Fe}]$ . Given that  $s$ -process elements are primarily produced by low-mass AGB stars ( $1.5\text{-}3 M_{\odot}$ ) over timescales of 0.3-2 Gyr (V. V. Smith et al. 2000), which is comparable to the  $\sim 1$  Gyr age difference between P1 and P2 (C. Clontz et al. 2024), the enhanced  $[\text{Ba}/\text{Fe}]$  in P2 could be naturally explained if P2 formed from gas enriched by the AGB ejecta of the earlier P1 stars.

### 5.2. Abundance Variations in 14 Subpopulations

The recent study by C. Clontz et al. (2025a) employed a clustering algorithm using both photometric chromosome diagram information and spectroscopic metallicity to identify 14 subpopulations in  $\omega$  Cen from the red giant branch to below the main sequence turnoff using the oMEGACat dataset. Some results from our abundance measurements were already presented in that work. In particular, the  $[\text{Na}/\text{Fe}]$  abundances of red giant and subgiant stars show that the subpopulations identified from the chromosome diagram can be consistently traced onto the subgiant branch. This correspondence enables subgiant ages (C. Clontz et al. 2024) to be inferred for each subpopulation. We focus on chemical abundance trends

with  $[\text{Fe}/\text{H}]$  in this subsection and discuss trends with age in the next subsection.

In this section, we combine the C. Clontz et al. (2025a) subpopulation classifications with our DD-PAYNE and literature abundance measurements to investigate chemical abundance variations among different subpopulations. The results are presented in Fig. 8 and Fig. 9, the top panel of Fig. 8 shows the RGB chromosome diagram labeled by subpopulations from C. Clontz et al. (2025a), and the remaining panels in these two figures illustrate the median abundance trends with metallicity. Here, circles represent oMEGACat DD-PAYNE samples and squares represent literature data. The literature source used for each element is the same as those in Fig. 7. For  $[\text{Na}/\text{Fe}]$ ,  $[\text{Ca}/\text{Fe}]$ , and  $[\text{Ba}/\text{Fe}]$ , we use abundance measurements from DD-PAYNE for all subpopulations. For  $[\text{C}/\text{Fe}]$ ,  $[\text{N}/\text{Fe}]$ , and  $[\text{O}/\text{Fe}]$ , we adopt DD-PAYNE measurements for the metal-rich subpopulations (10-13), and use literature measurements for the remaining subpopulations. For  $[\text{Mg}/\text{Fe}]$ , we use literature measurements for subpopulations 0 and 1 due to their low metallicities, where DD-PAYNE is less reliable, as well as for P2 subpopulations 2, 6, 9, and 10, where DD-PAYNE measurements show inconsistencies with the literature (as shown in Fig. 7). For reference, we list the number of DD-PAYNE and literature stars, along with the median chemical abundances used in Fig. 8 and Fig. 9, for all 14 subpopulations in Table 4.

As shown in Fig. 8 and Fig. 9,  $[\text{C}/\text{Fe}]$ ,  $[\text{N}/\text{Fe}]$ ,  $[\text{Na}/\text{Fe}]$ ,  $[\text{Ca}/\text{Fe}]$ , and  $[\text{Ba}/\text{Fe}]$  all show a nearly monotonic increase with metallicity. Overall, most P2 subpopulations (2, 6, 9, 10, 12, and 13) show enhanced enrichment in  $[\text{N}/\text{Fe}]$  and  $[\text{Na}/\text{Fe}]$ , and generally higher  $[\text{Ba}/\text{Fe}]$ , consistent with the three-stream trends in Fig. 7. Moreover, we compute the total C+N+O and find a tight increasing trend between  $[(\text{C}+\text{N}+\text{O})/\text{Fe}]$  and metallicity, with no significant differences between P1, Im, and P2, consistent with the results of A. F. Marino et al. (2012).

The  $\alpha$ -elements  $[\text{O}/\text{Fe}]$  and  $[\text{Mg}/\text{Fe}]$  show more complex patterns in Fig. 8 and Fig. 9.  $[\text{O}/\text{Fe}]$  shows a decreasing trend with metallicity from the most metal-poor to the metal-rich P1 subpopulations (subpops 0, 3, 4, and 8). The Im populations (1, 5, 7) continue this trend toward higher metallicities. In strong contrast with the P1 populations, but consistent with Fig. 7, the P2 subpopulations show a steep increase of  $[\text{O}/\text{Fe}]$  with metallicity. Combining the  $[\text{Na}/\text{Fe}]$  and  $[\text{O}/\text{Fe}]$  results, we find that all the P2 subpopulations are Na-enhanced and O-depleted compared to P1, exhibiting the classic Na-O anti-correlation expected from high-temperature hydrogen-burning (e.g., E. Carretta et al. 2009), consis-

**Table 4.** Number of stars and median chemical abundances of  $\omega$  Cen subpopulations

Pop.	ChD.	$N_{\text{DD-Payne}}$	$N_{\text{S24+}}$	[Fe/H]	[C/Fe]	[N/Fe]	[O/Fe]	[(C+N+O)/Fe]	[Na/Fe]	[Mg/Fe]	[Al/Fe]	[Ca/Fe]	[Ba/Fe]
(1)	(2)	(3)	(4)	(5)	(6)	(7)	(8)	(9)	(10)	(11)	(12)	(13)	(14)
0	P1	550	14	-1.98	-0.26*	0.14*	0.42*	0.30*	0.22	0.26*	-0.05*	0.24	-0.93
1	Im	724	13	-1.94	-0.34*	0.69*	0.20*	0.20*	0.25	0.18*	0.63*	0.23	-0.90
2	P2	528	7	-1.90	-0.11*	0.94*	-0.22*	0.23*	0.23	-0.29*	0.90*	0.27	-0.60
3	P1	594	24	-1.87	-0.23*	0.67*	0.36*	0.29*	0.08	0.19	0.02*	0.24	-0.54
4	P1	378	17	-1.78	-0.44*	0.52*	0.36*	0.24*	0.03	0.22	-0.23*	0.26	-0.25
5	Im	323	6	-1.78	-0.10*	1.03*	0.16*	0.29*	0.14	0.17	0.64*	0.28	-0.45
6	P2	494	5	-1.76	-0.09*	1.21*	-0.11*	0.31*	0.20	-0.32*	1.08*	0.30	-0.11
7	Im	168	7	-1.63	-0.14*	1.09*	0.25*	0.35*	0.20	0.25	0.42*	0.33	0.08
8	P1	177	5	-1.63	-0.25*	0.60*	0.32*	0.22*	0.01	0.26	0.00*	0.32	0.09
9	P2	509	7	-1.60	0.02*	1.21*	0.08*	0.36*	0.31	-0.04*	1.10*	0.31	0.33
10	P2	216	4	-1.37	0.09	1.14	0.13	0.46	0.52	0.12*	1.10*	0.32	0.73
11	P1	62	1	-1.37	0.25	0.76	0.48	0.47	0.16	0.36	0.07*	0.36	0.44
12	P2	184	2	-1.14	0.09	1.26	0.16	0.49	0.74	0.27	0.92*	0.37	0.61
13	P2	157	1	-0.83	0.14	1.51	0.28	0.64	0.89	0.43	0.76*	0.36	0.74

NOTE— Column (1): Subpopulation ID. Column (2): Chromosome-diagram class (P1, P2, or Im). Columns (3)–(4): Number of stars contributing to each subpopulation from DD-PAYNE (this work) and R. P. Schiavon et al. (2024), respectively. Columns (5)–(14): Median abundance of [Fe/H], [C/Fe], [N/Fe], [O/Fe], [C+N+O]/Fe, [Na/Fe], [Mg/Fe], [Al/Fe], [Ca/Fe], and [Ba/Fe]. Values are rounded to two decimal places; Population abundances marked with an asterisk (\*) are from the literature.

tent with previous studies (e.g. C. I. Johnson & C. A. Pilachowski 2010; A. F. Marino et al. 2011). We further confirm this by plotting the median [Na/Fe] and [O/Fe] for all subpopulations in Fig. 10. Similar to [O/Fe], [Mg/Fe] of all the P2 subpopulations are depleted which is consistent with Fig. 7. However, there is no decreasing trend of [Mg/Fe] with metallicity in P1 and Im subpopulations. Instead, they are located at very similar places with [Fe/H]  $\sim -1.75$  dex and [Mg/Fe]  $\sim 0.2$  dex. To investigate the potential Mg-Al anti-correlation, we take [Al/Fe] measurements from R. P. Schiavon et al. (2024) and plot the median [Al/Fe] and [Mg/Fe] distributions for all subpopulations in the bottom panel of Fig. 10, the results are also consistent with the literature (e.g., D. A. Alvarez Garay et al. 2024; A. C. Mason et al. 2025).

One notable exception to many of the trends discussed above is the most metal-rich P1 subpopulation (11), which is an outlier on the diagrams in several abundances. Population 11 follows some trends, such as those of Mg, Ba, and C+N+O with metallicity; it appears more like a discrete group with no clear continuity in C, N, O, and Na. This may indicate a distinct formation scenario for some subpopulations, which we will discuss further in Section 6.

### 5.3. Relation between Abundances and Age

In this section, we investigate the abundance-age relation for the subpopulations by combining results from C. Clontz et al. (2024) and C. Clontz et al. (2025a).

We focus especially on the behavior of P1, Im, and P2 groups given the reported  $\sim 1$  Gyr age gap between P1 and P2 reported in C. Clontz et al. (2025a). The results are shown in Fig. 11 and Fig. 12. For the light elements, we find that the 14 subpopulations show the tightest relation between [N/Fe] and age, with no significant differences between P1, Im, and P2. Similar to [N/Fe], [C/Fe] increases toward younger ages, except for the most metal-rich P1 subpopulation (11). Both [O/Fe] and [Mg/Fe] generally decrease with younger ages except for the two most-metal-rich P2 populations (12 and 13), which are enriched in both elements. We also show the relation between [(C+N+O)/Fe] and age in Fig. 11. Overall, the trend with age is weak, and apparent increase toward younger ages is largely driven by the most metal-rich population (13). This behavior likely reflects the opposite age trends of O relative to C and N, which reduces the net variation when the three elements are combined. [Na/Fe] generally shows an enrichment trend with younger age, though the P2 subpopulation 6 appears significantly younger than other groups at the same [Na/Fe] level. Another  $\alpha$ -element [Ca/Fe] and the heavy  $s$ -process element [Ba/Fe] exhibit increases toward younger ages, but with a much larger scatter than the relation with [Fe/H]. Notably, these two elements increases rapidly with younger age across subpopulations belonging to P1, Im, with enrichment timescales (0.13 Gyr for Im and 0.3 Gyr for P2). For

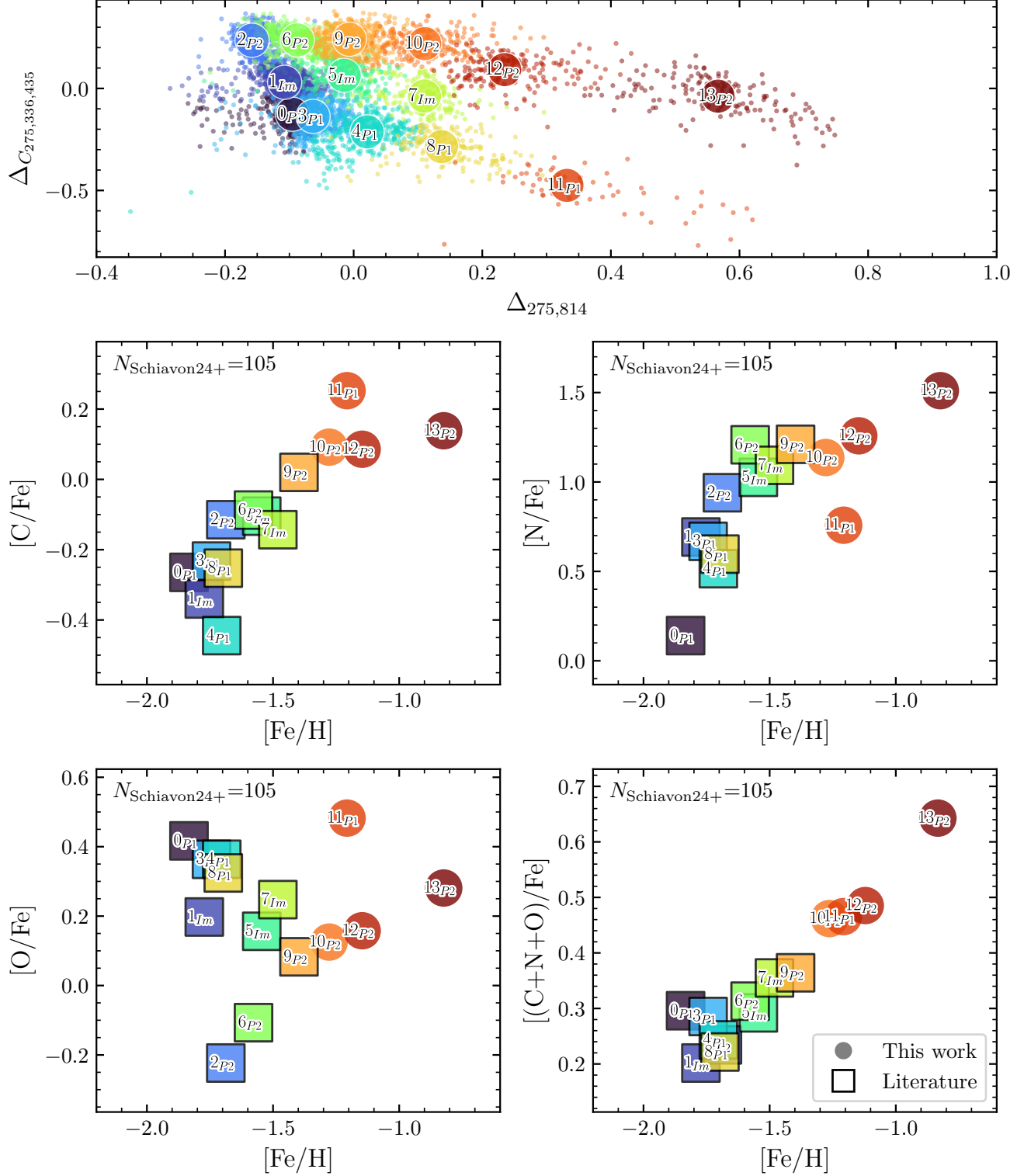


**Figure 8.** Chemical abundances of C, N, O, and (C+N+O) as a function of [Fe/H] for subpopulations defined by C. Clontz et al. (2025a). The top panel shows the chromosome diagram based on the photometry from C. Clontz et al. (2025a). For the remaining panels, we plot the median abundance as a function of metallicity for each element to illustrate the abundance-metallicity relations. Circles represent the DD-PAYNE measurements following the selection criteria in Section 4.1, and squares are literature results, with the number of literature stars used written in the top left corner.

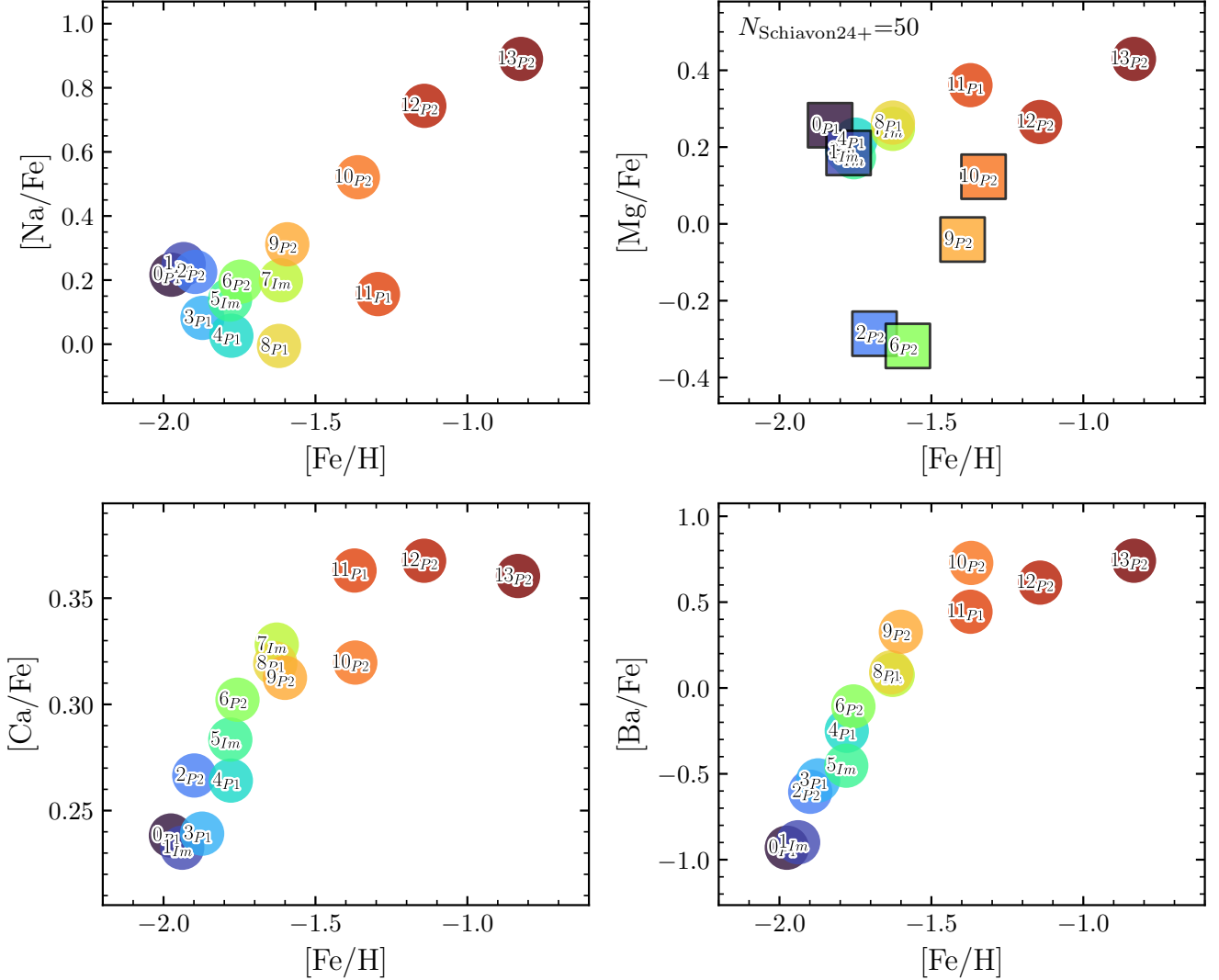


**Figure 9.** Same as Fig. 8 but for Na, Mg, Ca, and Ba.

[Ca/Fe], this could reflect the rapid enrichment due to Type II SNe (e.g., C. I. Johnson & C. A. Pilachowski 2010). For [Ba/Fe], this timescale is shorter than the lifetimes of low-mass AGB stars of 0.3-2 Gyr (V. V. Smith et al. 2000). If all subpopulations formed within the same environment, such rapid enrichment in [Ba/Fe] could be explained by contributions from massive rotating stars (L. J. Shingles et al. 2014; U. Frischknecht et al. 2016) as suggested by E. Dondoglio et al. (2026).

#### 5.4. Relative Enrichment of *s*-process and $\alpha$ -elements

To further investigate the enrichment history of  $\omega$  Cen, we examine the abundance ratios between the heavy *s*-process element Ba and the  $\alpha$ -elements Mg and Ca. In particular, we consider [Ba/Mg] and [Ba/Ca] as functions of both [Fe/H] and age. Such ratios have been shown to be sensitive tracers of relative enrichment

timescales between neutron-capture and core-collapse supernovae (Type II SNe) products (e.g., Á. Skúladóttir et al. 2019).

The results are shown in Fig. 13. Compared to [Ba/Fe], which contains Fe in both axes when plotted against [Fe/H], the [Ba/Ca] ratio provides a cleaner diagnostic of relative enrichment. Because Ca is primarily produced by Type II SNe and does not participate in light-element anti-correlations. The [Ba/Ca]-[Fe/H] relation (bottom left of Fig. 13) shows a smooth and continuous increasing trend, reinforcing the picture of progressive *s*-process enrichment with increasing metallicity. However, the [Ba/Mg]-[Fe/H] relation (top left of Fig. 13) shows more complexity due to the Mg-Al anti-correlation. Because Mg is depleted in P2 stars, the [Ba/Mg] ratios of P2 subpopulations appear more en-

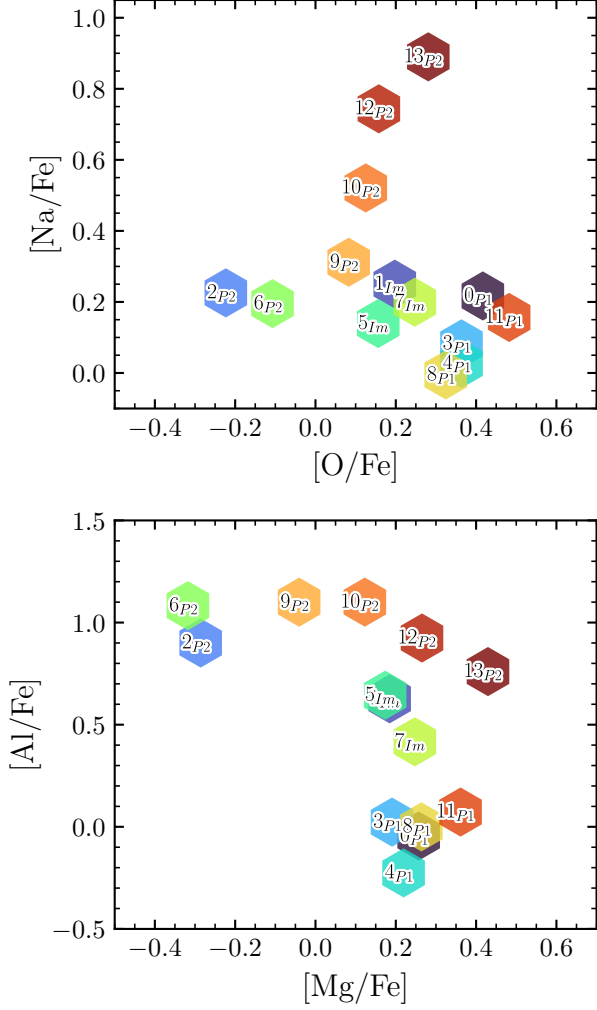


**Figure 10.** Na-O and Mg-Al anti-correlations for the 14 subpopulations identified by C. Clontz et al. (2025a).  $[O/Fe]$  and  $[Mg/Fe]$  values are derived from both the oMEGACat DD-PAYNE measurements and R. P. Schiavon et al. (2024), while  $[Al/Fe]$  is taken solely from R. P. Schiavon et al. (2024).  $[Na/Fe]$  is taken entirely from the oMEGACat DD-PAYNE measurements. All the corresponding values are listed in Table 4. Different from Fig. 9, the two axes in each panel may originate from different data sources. Therefore, a hexagon symbol is used for each subpopulation to indicate the combined measurements.

hanced relative to P1 and Im. This separation clearly illustrates the impact of light-element variations on chemical enrichment diagnostics and emphasizes the importance of using an  $\alpha$ -element such as Ca, which is not affected by proton-capture process, when assessing  $s$ -process enrichment.

The age relations in the right column of Fig. 13 provide further insight. Similar to the  $[Ba/Fe]$  trend in Fig. 12, both  $[Ba/Ca]$  and  $[Ba/Mg]$  show an overall increase to-

ward younger ages across the P1, Im, and P2 subpopulations, suggesting relatively more significant  $s$ -process enrichment compared to  $\alpha$ -element production. The enrichment in the younger subpopulations appears slower than in the older populations. However, unlike the tight relations with  $[Fe/H]$ , the age trends show larger scatter and do not follow a single sequence. When connecting subpopulations at similar metallicities (e.g., 0-1-2, 3-5-6, 4-7-9), the  $[Ba/Ca]$ -age diagram suggests possible evolutionary links consistent with a scenario in which multiple star-forming units at different metallicities experienced internal enrichment before merging into  $\omega$  Cen (e.g. C. Clontz et al. 2025a). Alternatively, grouping populations by P1, Im, and P2 reveals that older P1 and Im populations exhibit more rapid  $s$ -process enrichment relative to the younger P2 populations. In Section 6, we combine these abundance relations with  $[Fe/H]$  and age to evaluate the formation scenarios proposed in the literature, to investigate which scenario better matches our results.

## 6. EVALUATING THE COMPLEX FORMATION SCENARIOS OF OMEGA CENTAURI

The combination of our DD-PAYNE abundance measurements with literature data, together with the precise ages and subpopulation classifications from the oMEGACat survey, enables us to evaluate the formation scenarios proposed for  $\omega$  Cen. Any scenario must simultaneously explain the observed age distributions, chemical patterns, kinematics, and varied spatial distributions. In the following subsections, we discuss three main formation scenarios, highlighting both the observational evidence that supports them and that challenges them, to illustrate the difficulties in determining the formation history of  $\omega$  Cen.

### 6.1. Scenario 1: Two Environments, Separate Enrichment

One proposed model is that the P1 and P2 populations originated in separate environments and later merged. In this scenario, P1 and P2 are not evolutionarily related either because they formed in different locations or because they formed at different times. This scenario can naturally explain the  $\sim 1$  Gyr age gap between P1 and P2 (C. Clontz et al. 2024). In a single isolated system, it is difficult to maintain a relatively quiescent period with a duration of  $\sim 1$  Gyr, during which only Im stars were born. However, it can be explained if these two populations are formed at different time in different environments. A. C. Mason et al. (2025) found that the Im populations exhibits light-element patterns (such as the Mg-Al anticorrelation) typical of “normal” globular clusters.

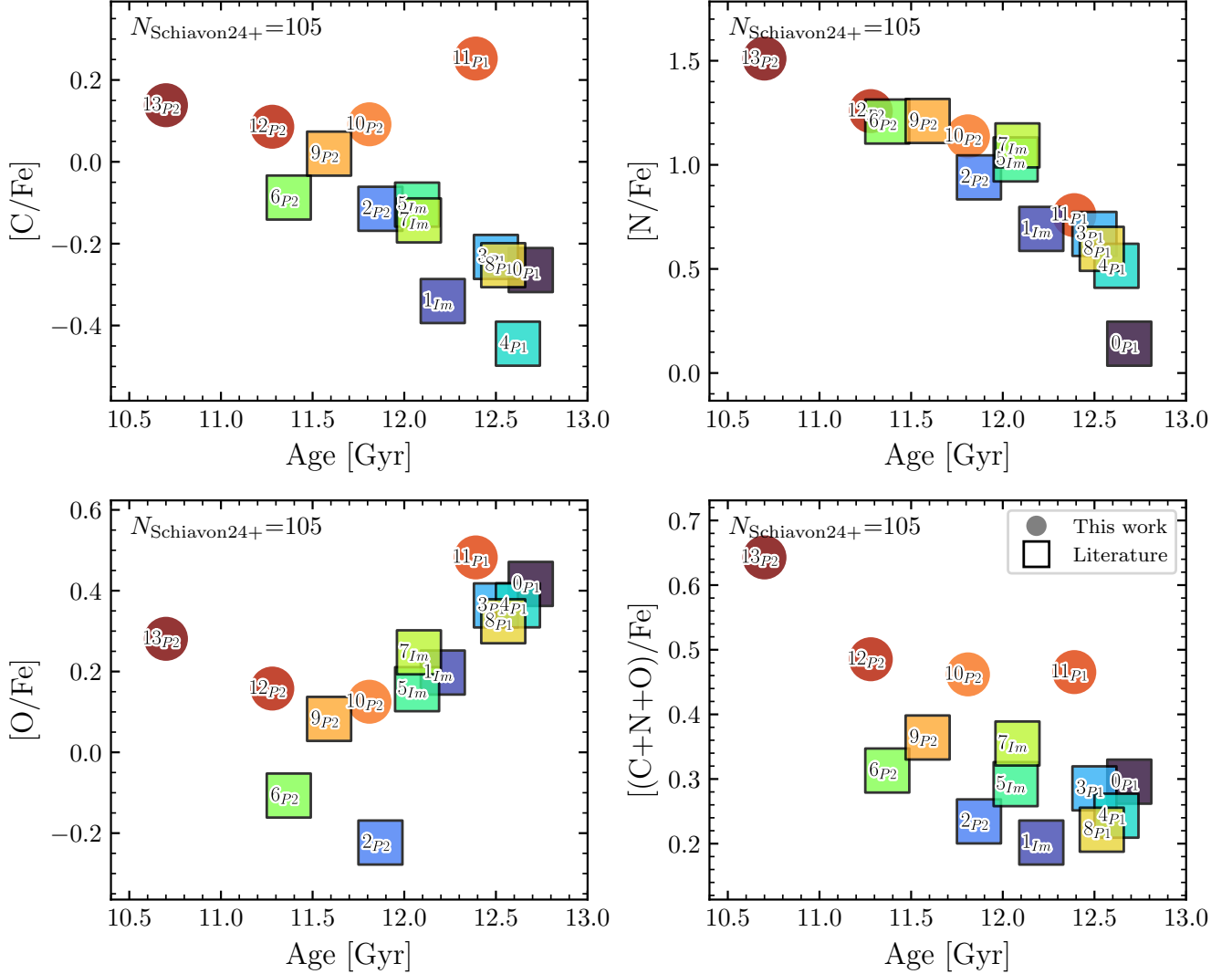


**Figure 11.** Chemical abundances of C, N, O, and (C+N+O) as a function of age for different subpopulations, plotted in the same way as Fig. 8 and Fig. 9. The median stellar ages for each population are adopted from C. Clontz et al. (2025a).

Therefore, the Im population could represent stars from an infalling globular cluster. Spatially, A. Sollima et al. (2007), A. Bellini et al. (2009), and E. Dondoglio et al. (2026) showed that P2/Helium-enriched subpopulations at all metallicities are more centrally concentrated than P1 (but also see A. Calamida et al. 2017, 2020, for a more complex picture). This would be an expectation of a merger event where the P2 cluster is a denser cluster and thus ends up more centrally concentrated.

However, our chemical abundance results present challenges to this “separate origins” scenario. If P1 and P2 formed in completely unrelated systems, their chemical enrichment histories should show no correlation. Instead, we observe a remarkably continuous set of chemical trends between the two groups. As shown in Fig. 8, Fig. 9, and Fig. 13,  $[(C+N+O)/Fe]$ ,  $[Ca/Fe]$ ,

$[Ba/Fe]$  (although some offset is seen between P1 and P2 at high metallicities), and  $[Ba/Ca]$  increase smoothly with metallicity rather than forming distinct enrichment tracks. We also find a tight correlation between  $[N/Fe]$  and age (Fig. 11). It would be very coincidental for the P2 population to continue the *s*-process and C+N+O enrichment from the P1 population. The observed chemical continuity instead suggests that the gas reservoir forming P2 should have been connected to, and chemically influenced by, the evolved stars of the P1 population.

A. C. Mason et al. (2025) proposed a modified scenario in which P1 formed first in the  $\omega$  Cen progenitor. The Im population is attributed to inspiralling gas-rich globular clusters, and the gas brought in by these systems subsequently fueled the formation of P2. This sce-

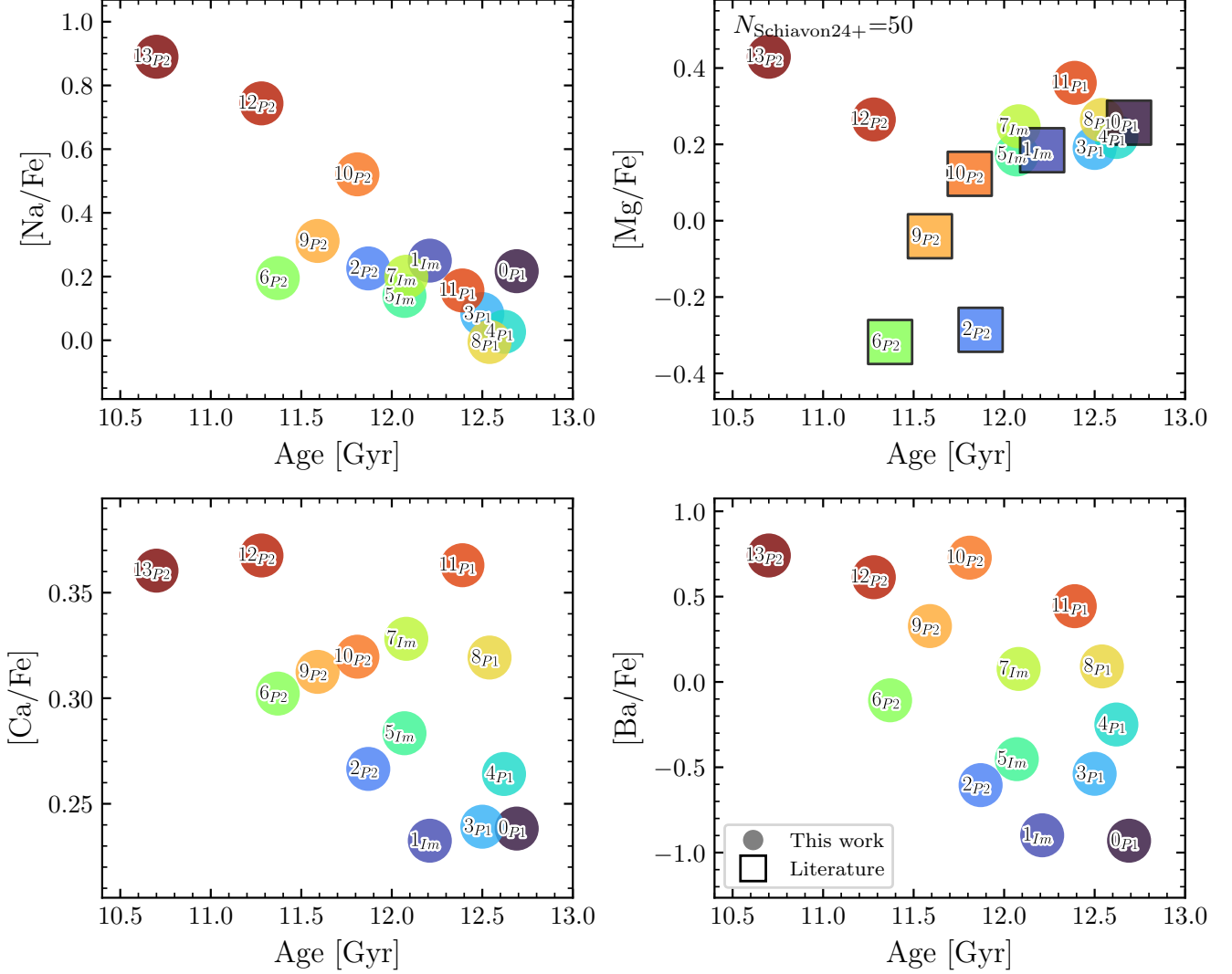


**Figure 12.** Same as Fig. 11 but for Na, Mg, Ca, and Ba.

nario can still explain the age differences among the P1, Im, and P2 populations, as the introduction of fresh gas and/or stars from external sources (e.g., via mergers) could have restarted star formation and led to the formation of P2 stars. It also accounts for the light-element patterns observed in Im stars (e.g., the Mg-Al anticorrelation). In this framework, the P1 and P2 populations can remain chemically connected because they formed at the same location; P2 stars would have formed from material polluted by evolved P1 stars and the infalling gas. To further verify this scenario, detailed chemical evolution modelling will be required to test whether it can reproduce the abundance trends observed in this study.

## 6.2. Scenario 2: Single-Environment Self-Enrichment

The second scenario suggests that P1, Im, and P2 formed within a single spatially coherent environment, as proposed by E. Dondoglio et al. (2026). In this scenario,  $\omega$  Cen experienced multiple star-formation episodes, with SNe ejecta being retained to explain the metallicity spread in both P1 and P2. The P2 population formed directly from gas polluted by the AGB ejecta of massive P1 stars.

If  $\omega$  Cen was the nucleus of a dwarf galaxy, the deep gravitational potential allows efficient retention of SNe and AGB ejecta. This scenario is supported by the chemical continuity with [Fe/H] and age already discussed above. The steady increase and extreme enrichment in *s*-process elements (e.g. [Ba/Fe]  $\sim$  1.0 dex) (C. I. Johnson & C. A. Pilachowski 2010; A. F. Marino

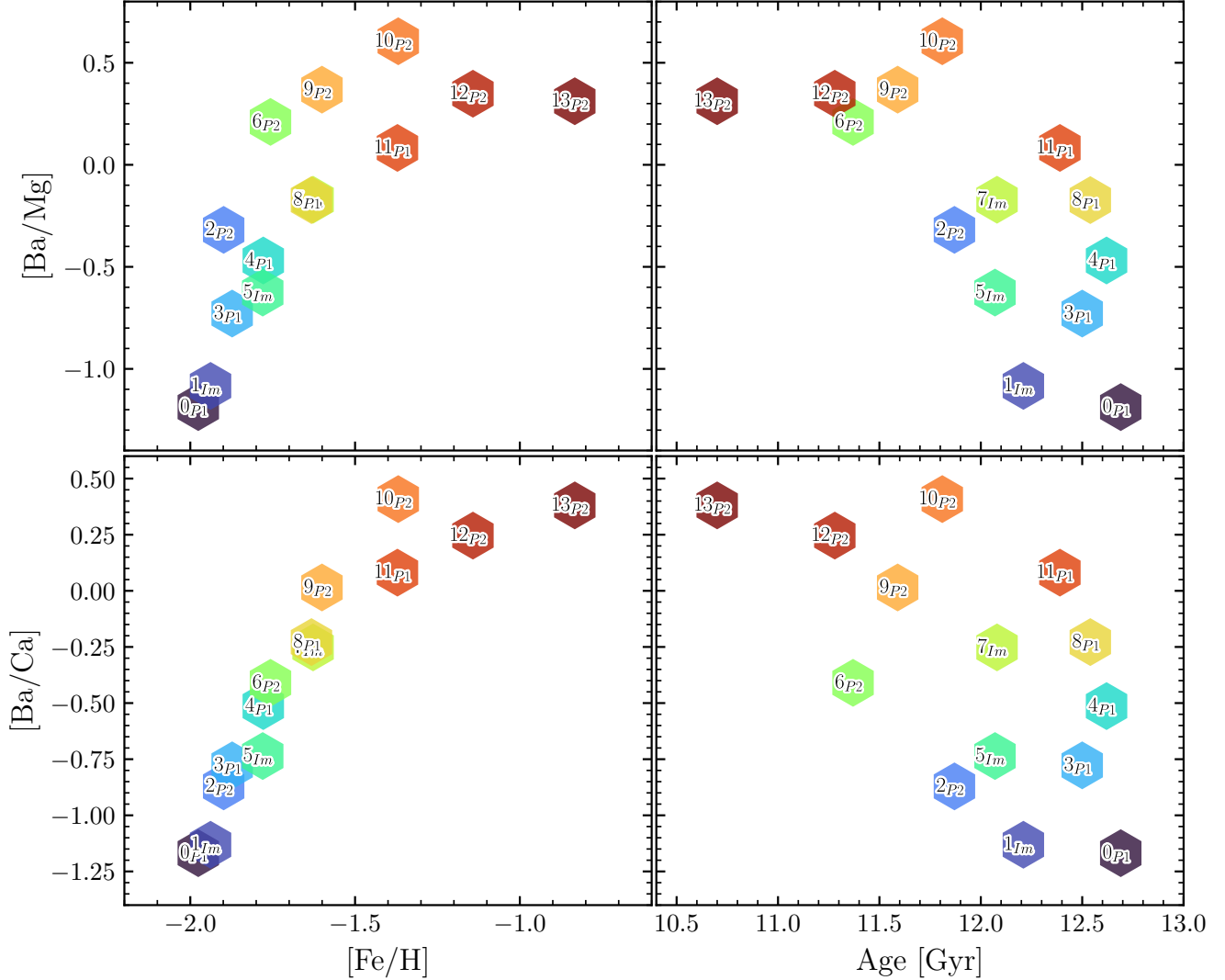


**Figure 13.** Ratios of the heavy  $s$ -process element Ba to  $\alpha$ -elements Mg and Ca as a function of  $[\text{Fe}/\text{H}]$  (left) and age (right). Top:  $[\text{Ba}/\text{Mg}]$ ; bottom:  $[\text{Ba}/\text{Ca}]$ . Data points represent median abundances of the 14 subpopulations calculated using  $[\text{Ba}/\text{Fe}]$ ,  $[\text{Ca}/\text{Fe}]$ , and  $[\text{Mg}/\text{Fe}]$  in Table 4; symbols and colors are consistent with Fig. 10.

et al. 2011, 2012) is consistent with enrichment from low- and intermediate-mass AGB stars ( $1.5\text{--}3 M_{\odot}$ ) over timescales of several hundred million years. There is also tight correlations of  $[(\text{C}+\text{N}+\text{O})/\text{Fe}]$ ,  $[\text{Ca}/\text{Fe}]$ ,  $[\text{Ba}/\text{Ca}]$  with metallicity and a tight  $[\text{N}/\text{Fe}]$ -age relation. Also favoring this scenario are the presence of Na-O and Mg-Al anti-correlations at a range of metallicities; these relations are similar to those found in typical globular clusters (R. G. Gratton et al. 2012). C. Clontz et al. (2025b) also found that helium increases with metallicity in the early (metal-poor) P2 sequence, which may be consistent with continuous helium production from massive AGB stars of the P1 population. E. Dondoglio et al. (2026) also cite the concentrated P2 morphology as evidence for this scenario, because centrally retained and

diluted ejecta would naturally lead to P2 stars forming preferentially in the cluster core. Nonetheless, this morphology alone cannot rule out a contribution from externally supplied gas (e.g., via inspiralling globular clusters, A. C. Mason et al. 2025).

Despite the above supporting evidence, this scenario faces several challenges. First, it is challenging to explain the large  $\sim 1$  Gyr separation between the main P1 and P2 star-formation episodes (C. Clontz et al. 2024, 2025a). Second (and related), it struggles to explain the low metallicities observed in the P2 population. If metallicity enrichment is continuous and P2 formed directly from the processed ejecta of P1, one would expect P2 to begin at a noticeably higher  $[\text{Fe}/\text{H}]$  than P1. Instead, we observe a significant overlap in  $[\text{Fe}/\text{H}]$  be-

tween P1 and P2, with the most metal-poor stars in P2 only 0.1 dex more metal-rich than the metal-poor tail in P1 (C. Clontz et al. 2025a; A. C. Mason et al. 2025). Reconciling this metallicity overlap would require substantial dilution of enriched material with pristine gas. This is difficult to achieve without removing key abundance signatures such as the continuous  $s$ -process and  $[(C+N+O)/Fe]$  enrichment and the Na-O and Mg-Al anti-correlations. Moreover, a large helium enhancement ( $\Delta Y \approx 0.15$ ) is already present at the lowest metallicity in P2, which is a challenge to explain with AGB enrichment (C. Clontz et al. 2025b). Furthermore, it is unclear why a second star-formation episode (P2) could restart with comparable intensity to P1 after such a long-delay, and why the Im population exhibits a noticeably narrower metallicity range (A. C. Mason et al. 2025; C. Clontz et al. 2025a). E. Dondoglio et al. (2026) suggested the Im population formed later from a mixture of ejecta from both P1 and P2 stars. However, this scenario would require Im stars to be present at all metallicities. In addition, the SGB ages (C. Clontz et al. 2024) indicate that the Im population has ages intermediate between P1 and P2, which is inconsistent with this formation pathway. In terms of subpopulations, Fig. 11 and Fig. 12 shows that not all the abundance-age relations are monotonic. If P1 and P2 evolved strictly within the same environment, it is hard to explain the complex, non-monotonic age abundance relations seen in these figures, particularly in  $[O/Fe]$ ,  $[Na/Fe]$ , and  $[Mg/Fe]$ . Finally, the most metal-rich populations in both P1 and P2 (populations 11 and 13 in Fig. 8, Fig. 9, Fig. 11, and Fig. 12) appear as outliers relative to the overall system. Their distinct chemistry are difficult to reconcile with a single-environment, purely self-enriched formation pathway.

### 6.3. Scenario 3: Multiple Environments, Concurrent Enrichment

A third possibility, suggested by the “two-stream” age-metallicity relation identified by C. Clontz et al. (2024), is that  $\omega$  Cen represents a complex assembly of multiple star-forming units (e.g., subpopulations 0-1-2, 3-5-6, 4-7-9) that evolved in parallel before merging. In this scenario, each major  $[Fe/H]$  group underwent its own localized chemical enrichment within the central regions of a dwarf galaxy but in slightly different localized environments (e.g., a central nucleus vs. surrounding clumps). This scenario attempts to bridge the gap between the first two. It naturally accommodates the tight age-metallicity sequence seen in Fig. 4 of C. Clontz et al. (2024) and also explains the large metallicity spread at a given age and the overlap of metal-

poor tail between P1 and P2. Moreover, it alleviates the requirement for strictly monotonic enrichment in the abundance-age relations. The small differences in light-elemental abundances and anti-correlations at different metallicities could be due to each group experiencing its own globular-cluster-like enrichment cycle independently and creating its own “second-generation” stars.

However, like Scenario 1, this scenario raises questions regarding the apparent chemical continuity between the different metallicity groups. Although combined abundance trends with  $[Fe/H]$  from all the star-forming units can be relatively tight if formed in the same dwarf galaxy (e.g., M. Shetrone et al. 2026), the continuous and extended chromosome sequences of P1 and P2 (C. Clontz et al. 2025b) suggest a level of coordinated enrichment that may be difficult to reconcile with independent evolution of multiple star-forming units. Instead, they can be more easily explained if the metal-rich populations (whether in P1 or P2) formed from the core-collapse supernovae ejecta of the metal-poor populations within the same sequence. Moreover, the extreme helium enhancement observed across all P2 populations is not typically seen in independent and less massive systems. Furthermore, this scenario does not account for all identified subpopulations. In particular, the absence of Im stars at the highest metallicities leaves populations 10, 11, 12, and 13 without a clear evolutionary connection.

### 6.4. Summary of All the Scenarios

As detailed in the previous sections, no single formation scenario presented here or in the literature provides a full explanation for the complex formation history of  $\omega$  Cen. By combining the observational evidence from our DD-PAYNE and literature results, we identify five key factors that make the interpretation of  $\omega$  Cen’s formation history challenging:

1. The large age gap ( $\sim 1$  Gyr) between two main star formation episodes P1 and P2.
2. The significant metallicity overlap between P1 and P2, with Im in between.
3. The continuous chemical enrichment in N, total C+N+O, Ca, and Ba across the P1, Im, and P2 populations.
4. The extreme helium enrichment in the P2 population even at its lowest metallicities.
5. The origin of Im populations with relatively narrower metallicity spreads compared to P1 and P2.

Another possibility to explain the age gap is that the later populations (Im and/or P2) were triggered by close

passages or disk crossings of the progenitor dwarf galaxy through the Milky Way. In this scenario, tidal interactions compress or funnel gas toward the central regions, inducing new separated star-formation episodes. After repeated interactions, the outer regions of the dwarf galaxy would be stripped, leaving only the remnant nucleus observed today as  $\omega$  Cen. This scenario preserves a common nuclear environment while allowing externally triggered star formation, and such tidally induced nuclear starbursts have been demonstrated in numerical simulations (e.g., K. Bekki & K. C. Freeman 2003).

In addition, several other important factors have not been considered. From a kinematic perspective, G. Cordoni et al. (2020) and T. Ziliotto et al. (2025) showed that P2 stars exhibit higher radial anisotropy than P1 stars. This feature can be interpreted in multiple ways. P2 may have formed from infalling material or an accreted subsystem, or it may reflect gas ejected from the P1 population falling back toward the cluster center with slightly different kinematic properties. However, any present-day kinematic differences are not necessarily primordial, as radial anisotropy can be imprinted during the subsequent long-term dynamical evolution of the cluster (e.g., M. A. Tiongco et al. 2019; F. I. Aros et al. 2025). The recent confirmation of an intermediate-mass black hole (IMBH) in the center of  $\omega$  Cen (M. Häberle et al. 2024a) may also introduce additional complexity. The IMBH may provide a missing link to the extreme helium enrichment of P2 (C. Clontz et al. 2025b), potentially through events such as the formation of supermassive stars (SMS) (e.g. M. Gieles et al. 2025) or long-lived “immortal” stars in an AGN-like disk that happened between the formation of P1 and P2 (e.g. A. J. Dittmann et al. 2023), or the formation and rejuvenation of massive stars via dynamical interactions in the dense cluster core (e.g., A. Rantala et al. 2025). The IMBH could further influence chemical enrichment indirectly by modifying the retention, mixing, and redistribution of stellar ejecta in the central regions.

## 7. SUMMARY

In this work, we apply the neural network model DD-PAYNE to MUSE spectra of 7,302 RGB stars in the oMEGACat dataset. We derived chemical abundances of [C/Fe], [N/Fe], [O/Fe] at the metal-rich end ( $[\text{Fe}/\text{H}]_{\text{uncal}} > -1.0$  dex), [Mg/Fe] for  $[\text{Fe}/\text{H}]_{\text{uncal}} > -1.5$  dex, and [Na/Fe], [Ca/Fe], and [Ba/Fe] across the full metallicity range of  $\omega$  Cen. By combining our measurements with high-resolution spectroscopic literature, we constructed the most comprehensive chemical abundance distributions of  $\omega$  Cen on the chromosome diagram to date (Fig. 6). We investigated abundance trends

with metallicity and age by separating stars into the widely adopted P1, Intermediate, and P2 populations (Fig. 7), as well as the 14 subpopulations identified by C. Clontz et al. (2025a) (Fig. 8-13). Our main results are summarized as follows:

1. P2 stars are consistently enhanced in [N/Fe] and [Na/Fe] and depleted in [O/Fe] and [Mg/Fe] compared to P1 stars at similar metallicities.
2. The Im populations occupy an intermediate position between P1 and P2 in chemical space but largely follow the chemical trends of P1.
3. The total [(C+N+O)/Fe],  $\alpha$ -element [Ca/Fe], and the *s*-process element [Ba/Fe] increase continuously with metallicity across the P1 and P2 populations, suggesting a related formation environment.
4. P2 stars show a clear [Ba/Fe] offset relative to the P1 and Intermediate populations.
5. Analysis of the 14 subpopulations reveals a strong correlation between [N/Fe] and stellar age, suggesting nitrogen acts as a tracer for the cluster’s enrichment history. [Ba/Fe] also exhibits a weaker dependence on age, consistent with delayed enrichment from low- and intermediate-mass AGB stars.
6. The [Ba/Ca] ratio increases smoothly with metallicity and shows an overall increase toward younger ages, indicating relatively stronger neutron-capture enrichment relative to core-collapse supernovae production.

Furthermore, we evaluated three proposed formation scenarios for  $\omega$  Cen using observational evidence of chemical abundances, spatial distributions, kinematics, and ages. This analysis demonstrates the difficulties in reconciling their constraints to identify the definitive formation history of  $\omega$  Cen.

Our study demonstrates that machine learning approaches applied to integral-field spectroscopy can effectively recover detailed chemical abundances in crowded environments where traditional multi-object spectroscopy is limited. The resulting dataset provides valuable new constraints for chemical evolution models aiming to reconstruct the formation history of  $\omega$  Cen.

The application of DD-PAYNE to  $\omega$  Cen in this work demonstrates the feasibility of measuring chemical abundances from MUSE spectra in crowded stellar fields. This method can be extended to the wider MUSE globular cluster survey (S. Kamann et al. 2018), which includes observations of the central regions of 25 clusters.

Analyzing these datasets will provide spatially resolved abundance maps and provide essential constraints on the chemical patterns of multiple populations.

A detailed comparison between the observed abundance trends and theoretical stellar yields will be necessary to fully constrain the enrichment pathways of helium, light, and *s*-process elements. In particular, updated yields for massive stars (e.g., M. Limongi & A. Chieffi 2018) and AGB stars at low metallicities with different masses (e.g., A. I. Karakas & J. C. Lattanzio 2014) and their enrichment timescales are needed to better constrain the enrichment for the helium, light, and *s*-process elements as discussed in Section 6.

Moreover, the abundance measurements can be improved with updates to the DD-PAYNE model. New training sets using APOGEE DR19 (SDSS Collaboration et al. 2025) and GALAH DR4 (S. Buder et al. 2025) will provide more precise abundance measurements and better coverage of metal-poor stars ( $[\text{Fe}/\text{H}] < -1.5$ ). The upgraded TRANSFORMERPAYNE (T. Róžański et al. 2025) model could also provide more robust and accurate abundance estimates from MUSE spectra.

## ACKNOWLEDGMENTS

We thank C. Foster, M. R. Hayden, C. Manea, S. Martell, M. McKenzie, and J. van de Sande for useful discussions. Z.W., A.C.S., and C.C. acknowledge the support from a *Hubble Space Telescope* grant GO-16777. AFK acknowledges funding from the Austrian Science Fund (FWF) [grant DOI 10.55776/ESP542]. This work is done using Yoga (<https://yoga-server.github.io/>), a privately built Linux server for astronomical computing.

*Facilities:* HST(STScI), VLT:Yepun (MUSE)

*Software:* Astropy (Astropy Collaboration et al. 2013, 2018), Numpy (C. R. Harris et al. 2020), Scipy (P. Virtanen et al. 2020), Matplotlib (J. D. Hunter 2007), DD-PAYNE (Y.-S. Ting et al. 2017; M. Xiang et al. 2019)

## REFERENCES

- Abdurro’uf, Accetta, K., Aerts, C., et al. 2022, ApJS, 259, 35, doi: [10.3847/1538-4365/ac4414](https://doi.org/10.3847/1538-4365/ac4414)
- Alvarez Garay, D. A., Mucciarelli, A., Bellazzini, M., Lardo, C., & Ventura, P. 2024, A&A, 681, A54, doi: [10.1051/0004-6361/202347834](https://doi.org/10.1051/0004-6361/202347834)
- Alvarez Garay, D. A., Mucciarelli, A., Lardo, C., Bellazzini, M., & Merle, T. 2022, ApJL, 928, L11, doi: [10.3847/2041-8213/ac5ccf](https://doi.org/10.3847/2041-8213/ac5ccf)
- Anderson, J., & van der Marel, R. P. 2010, ApJ, 710, 1032, doi: [10.1088/0004-637X/710/2/1032](https://doi.org/10.1088/0004-637X/710/2/1032)
- Aros, F. I., Vesperini, E., & Dalessandro, E. 2025, A&A, 699, A44, doi: [10.1051/0004-6361/202453155](https://doi.org/10.1051/0004-6361/202453155)
- Asa’d, R., Hernandez, S., John, J. M., et al. 2024, AJ, 167, 265, doi: [10.3847/1538-3881/ad3f1b](https://doi.org/10.3847/1538-3881/ad3f1b)
- Astropy Collaboration, Robitaille, T. P., Tollerud, E. J., et al. 2013, A&A, 558, A33, doi: [10.1051/0004-6361/201322068](https://doi.org/10.1051/0004-6361/201322068)
- Astropy Collaboration, Price-Whelan, A. M., Sipócz, B. M., et al. 2018, AJ, 156, 123, doi: [10.3847/1538-3881/aabc4f](https://doi.org/10.3847/1538-3881/aabc4f)
- Bacon, R., Accardo, M., Adjali, L., et al. 2010, in Society of Photo-Optical Instrumentation Engineers (SPIE) Conference Series, Vol. 7735, Ground-based and Airborne Instrumentation for Astronomy III, ed. I. S. McLean, S. K. Ramsay, & H. Takami, 773508, doi: [10.1117/12.856027](https://doi.org/10.1117/12.856027)
- Bastian, N., & Lardo, C. 2018, ARA&A, 56, 83, doi: [10.1146/annurev-astro-081817-051839](https://doi.org/10.1146/annurev-astro-081817-051839)
- Bedin, L. R., Piotto, G., Anderson, J., et al. 2004, ApJL, 605, L125, doi: [10.1086/420847](https://doi.org/10.1086/420847)
- Bekki, K., & Freeman, K. C. 2003, MNRAS, 346, L11, doi: [10.1046/j.1365-2966.2003.07275.x](https://doi.org/10.1046/j.1365-2966.2003.07275.x)
- Bellini, A., Milone, A. P., Anderson, J., et al. 2017, ApJ, 844, 164, doi: [10.3847/1538-4357/aa7b7e](https://doi.org/10.3847/1538-4357/aa7b7e)
- Bellini, A., Piotto, G., Bedin, L. R., et al. 2009, A&A, 507, 1393, doi: [10.1051/0004-6361/200912757](https://doi.org/10.1051/0004-6361/200912757)
- Buder, S., Asplund, M., Duong, L., et al. 2018, MNRAS, 478, 4513, doi: [10.1093/mnras/sty1281](https://doi.org/10.1093/mnras/sty1281)
- Buder, S., Kos, J., Wang, X. E., et al. 2025, PASA, 42, e051, doi: [10.1017/pasa.2025.26](https://doi.org/10.1017/pasa.2025.26)
- Calamida, A., Strampelli, G., Rest, A., et al. 2017, AJ, 153, 175, doi: [10.3847/1538-3881/aa6397](https://doi.org/10.3847/1538-3881/aa6397)
- Calamida, A., Zocchi, A., Bono, G., et al. 2020, ApJ, 891, 167, doi: [10.3847/1538-4357/ab77c0](https://doi.org/10.3847/1538-4357/ab77c0)
- Carretta, E., Bragaglia, A., Gratton, R. G., et al. 2009, A&A, 505, 117, doi: [10.1051/0004-6361/200912096](https://doi.org/10.1051/0004-6361/200912096)
- Clontz, C., Seth, A. C., Dotter, A., et al. 2024, ApJ, 977, 14, doi: [10.3847/1538-4357/ad8621](https://doi.org/10.3847/1538-4357/ad8621)
- Clontz, C., Seth, A. C., Wang, Z., et al. 2025a, arXiv e-prints, arXiv:2510.26341, doi: [10.48550/arXiv.2510.26341](https://doi.org/10.48550/arXiv.2510.26341)

- Clontz, C., Seth, A. C., Wang, Z., et al. 2025b, *ApJ*, 984, 162, doi: [10.3847/1538-4357/adc1c5](https://doi.org/10.3847/1538-4357/adc1c5)
- Cordonni, G., Milone, A. P., Marino, A. F., et al. 2020, *ApJ*, 898, 147, doi: [10.3847/1538-4357/aba04b](https://doi.org/10.3847/1538-4357/aba04b)
- Deng, L.-C., Newberg, H. J., Liu, C., et al. 2012, *Research in Astronomy and Astrophysics*, 12, 735, doi: [10.1088/1674-4527/12/7/003](https://doi.org/10.1088/1674-4527/12/7/003)
- Dittmann, A. J., Jermyn, A. S., & Cantiello, M. 2023, *ApJ*, 946, 56, doi: [10.3847/1538-4357/acacf2](https://doi.org/10.3847/1538-4357/acacf2)
- Dondoglio, E., Milone, A. P., Marino, A. F., et al. 2026, *A&A*, 705, A2, doi: [10.1051/0004-6361/202556545](https://doi.org/10.1051/0004-6361/202556545)
- Dotter, A., Conroy, C., Cargile, P., & Asplund, M. 2017, *ApJ*, 840, 99, doi: [10.3847/1538-4357/aa6d10](https://doi.org/10.3847/1538-4357/aa6d10)
- Dupree, A. K., & Avrett, E. H. 2013, *ApJL*, 773, L28, doi: [10.1088/2041-8205/773/2/L28](https://doi.org/10.1088/2041-8205/773/2/L28)
- Dupree, A. K., Strader, J., & Smith, G. H. 2011, *ApJ*, 728, 155, doi: [10.1088/0004-637X/728/2/155](https://doi.org/10.1088/0004-637X/728/2/155)
- Ferraro, F. R., Sollima, A., Pancino, E., et al. 2004, *ApJL*, 603, L81, doi: [10.1086/383149](https://doi.org/10.1086/383149)
- Freeman, K. C., & Rodgers, A. W. 1975, *ApJL*, 201, L71, doi: [10.1086/181945](https://doi.org/10.1086/181945)
- Frischknecht, U., Hirschi, R., Pignatari, M., et al. 2016, *MNRAS*, 456, 1803, doi: [10.1093/mnras/stv2723](https://doi.org/10.1093/mnras/stv2723)
- Gieles, M., Padoan, P., Charbonnel, C., Vink, J. S., & Ramírez-Galeano, L. 2025, *MNRAS*, 544, 483, doi: [10.1093/mnras/staf1314](https://doi.org/10.1093/mnras/staf1314)
- Gratton, R. G., Carretta, E., & Bragaglia, A. 2012, *A&A Rv*, 20, 50, doi: [10.1007/s00159-012-0050-3](https://doi.org/10.1007/s00159-012-0050-3)
- Gratton, R. G., Johnson, C. I., Lucatello, S., D'Orazi, V., & Pilachowski, C. 2011, *A&A*, 534, A72, doi: [10.1051/0004-6361/201117093](https://doi.org/10.1051/0004-6361/201117093)
- Häberle, M., Neumayer, N., Seth, A., et al. 2024a, *Nature*, 631, 285, doi: [10.1038/s41586-024-07511-z](https://doi.org/10.1038/s41586-024-07511-z)
- Häberle, M., Neumayer, N., Bellini, A., et al. 2024b, *ApJ*, 970, 192, doi: [10.3847/1538-4357/ad47f5](https://doi.org/10.3847/1538-4357/ad47f5)
- Häberle, M., Neumayer, N., Clontz, C., et al. 2025, *ApJ*, 983, 95, doi: [10.3847/1538-4357/adbe67](https://doi.org/10.3847/1538-4357/adbe67)
- Harris, C. R., Millman, K. J., van der Walt, S. J., et al. 2020, *Nature*, 585, 357, doi: [10.1038/s41586-020-2649-2](https://doi.org/10.1038/s41586-020-2649-2)
- Hayden, M. R., Bovy, J., Holtzman, J. A., et al. 2015, *ApJ*, 808, 132, doi: [10.1088/0004-637X/808/2/132](https://doi.org/10.1088/0004-637X/808/2/132)
- Hema, B. P., & Pandey, G. 2014, *ApJL*, 792, L28, doi: [10.1088/2041-8205/792/2/L28](https://doi.org/10.1088/2041-8205/792/2/L28)
- Hema, B. P., Pandey, G., Kurucz, R. L., & Allende Prieto, C. 2020, *ApJ*, 897, 32, doi: [10.3847/1538-4357/ab93bd](https://doi.org/10.3847/1538-4357/ab93bd)
- Hema, B. P., Pandey, G., & Srianand, R. 2018, *ApJ*, 864, 121, doi: [10.3847/1538-4357/aad696](https://doi.org/10.3847/1538-4357/aad696)
- Hunter, J. D. 2007, *Computing in Science and Engineering*, 9, 90, doi: [10.1109/MCSE.2007.55](https://doi.org/10.1109/MCSE.2007.55)
- Ideta, M., & Makino, J. 2004, *ApJL*, 616, L107, doi: [10.1086/426505](https://doi.org/10.1086/426505)
- Johnson, C. I., & Pilachowski, C. A. 2010, *ApJ*, 722, 1373, doi: [10.1088/0004-637X/722/2/1373](https://doi.org/10.1088/0004-637X/722/2/1373)
- Joo, S.-J., & Lee, Y.-W. 2013, *ApJ*, 762, 36, doi: [10.1088/0004-637X/762/1/36](https://doi.org/10.1088/0004-637X/762/1/36)
- Kacharov, N., & Koch, A. 2013, *Mem. Soc. Astron. Italiana*, 84, 224, doi: [10.48550/arXiv.1301.2153](https://doi.org/10.48550/arXiv.1301.2153)
- Kamann, S., Wisotzki, L., & Roth, M. M. 2013, *A&A*, 549, A71, doi: [10.1051/0004-6361/201220476](https://doi.org/10.1051/0004-6361/201220476)
- Kamann, S., Husser, T.-O., Dreizler, S., et al. 2018, *MNRAS*, 473, 5591, doi: [10.1093/mnras/stx2719](https://doi.org/10.1093/mnras/stx2719)
- Karakas, A. I., & Lattanzio, J. C. 2014, *PASA*, 31, e030, doi: [10.1017/pasa.2014.21](https://doi.org/10.1017/pasa.2014.21)
- King, I. R., Bedin, L. R., Cassisi, S., et al. 2012, *AJ*, 144, 5, doi: [10.1088/0004-6256/144/1/5](https://doi.org/10.1088/0004-6256/144/1/5)
- Kurucz, R. 1993, *Robert Kurucz CD-ROM*, 18
- Kurucz, R. L. 1970, *SAO Special Report*, 309
- Kurucz, R. L. 2005, *Memorie della Societa Astronomica Italiana Supplementi*, 8, 14
- Lardo, C., Pancino, E., Mucciarelli, A., & Milone, A. P. 2012, *A&A*, 548, A107, doi: [10.1051/0004-6361/201220129](https://doi.org/10.1051/0004-6361/201220129)
- Latour, M., Calamida, A., Husser, T.-O., et al. 2021, *A&A*, 653, L8, doi: [10.1051/0004-6361/202141791](https://doi.org/10.1051/0004-6361/202141791)
- Latour, M., Kamann, S., Martocchia, S., et al. 2025, *A&A*, 694, A248, doi: [10.1051/0004-6361/202452420](https://doi.org/10.1051/0004-6361/202452420)
- Lee, Y.-W., Joo, J.-M., Sohn, Y.-J., et al. 1999, *Nature*, 402, 55, doi: [10.1038/46985](https://doi.org/10.1038/46985)
- Limongi, M., & Chieffi, A. 2018, *ApJS*, 237, 13, doi: [10.3847/1538-4365/aacb24](https://doi.org/10.3847/1538-4365/aacb24)
- Liu, X.-W., Zhao, G., & Hou, J.-L. 2015, *Research in Astronomy and Astrophysics*, 15, 1089, doi: [10.1088/1674-4527/15/8/001](https://doi.org/10.1088/1674-4527/15/8/001)
- Liu, X.-W., Yuan, H.-B., Huo, Z.-Y., et al. 2014, in *IAU Symposium*, Vol. 298, *Setting the scene for Gaia and LAMOST*, ed. S. Feltzing, G. Zhao, N. A. Walton, & P. Whitelock, 310–321, doi: [10.1017/S1743921313006510](https://doi.org/10.1017/S1743921313006510)
- Majewski, S. R., Nidever, D. L., Smith, V. V., et al. 2012, *ApJL*, 747, L37, doi: [10.1088/2041-8205/747/2/L37](https://doi.org/10.1088/2041-8205/747/2/L37)
- Marino, A. F., Milone, A. P., Piotto, G., et al. 2011, *ApJ*, 731, 64, doi: [10.1088/0004-637X/731/1/64](https://doi.org/10.1088/0004-637X/731/1/64)
- Marino, A. F., Milone, A. P., Piotto, G., et al. 2012, *ApJ*, 746, 14, doi: [10.1088/0004-637X/746/1/14](https://doi.org/10.1088/0004-637X/746/1/14)
- Marino, A. F., Milone, A. P., Renzini, A., et al. 2019, *MNRAS*, 487, 3815, doi: [10.1093/mnras/stz1415](https://doi.org/10.1093/mnras/stz1415)
- Mason, A. C., Schiavon, R. P., Kamann, S., et al. 2025, *arXiv e-prints*, arXiv:2504.06341, doi: [10.48550/arXiv.2504.06341](https://doi.org/10.48550/arXiv.2504.06341)

- Mészáros, S., Masseron, T., García-Hernández, D. A., et al. 2020, *MNRAS*, 492, 1641, doi: [10.1093/mnras/stz3496](https://doi.org/10.1093/mnras/stz3496)
- Mészáros, S., Masseron, T., Fernández-Trincado, J. G., et al. 2021, *MNRAS*, 505, 1645, doi: [10.1093/mnras/stab1208](https://doi.org/10.1093/mnras/stab1208)
- Milone, A. P., Marino, A. F., Bedin, L. R., et al. 2017a, *MNRAS*, 469, 800, doi: [10.1093/mnras/stx836](https://doi.org/10.1093/mnras/stx836)
- Milone, A. P., Piotto, G., Renzini, A., et al. 2017b, *MNRAS*, 464, 3636, doi: [10.1093/mnras/stw2531](https://doi.org/10.1093/mnras/stw2531)
- Neumayer, N., Seth, A., & Böker, T. 2020, *A&A Rv*, 28, 4, doi: [10.1007/s00159-020-00125-0](https://doi.org/10.1007/s00159-020-00125-0)
- Nitschai, M. S., Neumayer, N., Clontz, C., et al. 2023, *ApJ*, 958, 8, doi: [10.3847/1538-4357/acf5db](https://doi.org/10.3847/1538-4357/acf5db)
- Nitschai, M. S., Neumayer, N., Häberle, M., et al. 2024, *ApJ*, 970, 152, doi: [10.3847/1538-4357/ad5289](https://doi.org/10.3847/1538-4357/ad5289)
- Norris, J., & Bessell, M. S. 1975, *ApJL*, 201, L75, doi: [10.1086/181946](https://doi.org/10.1086/181946)
- Norris, J. E., & Da Costa, G. S. 1995, *ApJ*, 447, 680, doi: [10.1086/175909](https://doi.org/10.1086/175909)
- Origlia, L., Ferraro, F. R., Bellazzini, M., & Pancino, E. 2003, *ApJ*, 591, 916, doi: [10.1086/375363](https://doi.org/10.1086/375363)
- Pancino, E., Ferraro, F. R., Bellazzini, M., Piotto, G., & Zoccali, M. 2000, *ApJL*, 534, L83, doi: [10.1086/312658](https://doi.org/10.1086/312658)
- Piotto, G., Villanova, S., Bedin, L. R., et al. 2005, *ApJ*, 621, 777, doi: [10.1086/427796](https://doi.org/10.1086/427796)
- Rantala, A., Lahén, N., Naab, T., Escobar, G. J., & Iorio, G. 2025, *MNRAS*, 543, 2130, doi: [10.1093/mnras/staf1519](https://doi.org/10.1093/mnras/staf1519)
- Różański, T., Ting, Y.-S., & Jabłońska, M. 2025, *ApJ*, 980, 66, doi: [10.3847/1538-4357/ad9b99](https://doi.org/10.3847/1538-4357/ad9b99)
- Sandford, N. R., Weisz, D. R., & Ting, Y.-S. 2020, *ApJS*, 249, 24, doi: [10.3847/1538-4365/ab9cb0](https://doi.org/10.3847/1538-4365/ab9cb0)
- Sbordone, L., Salaris, M., Weiss, A., & Cassisi, S. 2011, *A&A*, 534, A9, doi: [10.1051/0004-6361/201116714](https://doi.org/10.1051/0004-6361/201116714)
- Schiavon, R. P., Phillips, S. G., Myers, N., et al. 2024, *MNRAS*, 528, 1393, doi: [10.1093/mnras/stad3020](https://doi.org/10.1093/mnras/stad3020)
- SDSS Collaboration, Adamane Pallathadka, G., Aghakhanloo, M., et al. 2025, arXiv e-prints, arXiv:2507.07093, doi: [10.48550/arXiv.2507.07093](https://doi.org/10.48550/arXiv.2507.07093)
- Shetrone, M., Beaton, R. L., Hayes, C. R., et al. 2026, *ApJ*, 998, 117, doi: [10.3847/1538-4357/ae27c5](https://doi.org/10.3847/1538-4357/ae27c5)
- Shingles, L. J., Karakas, A. I., Hirschi, R., et al. 2014, *ApJ*, 795, 34, doi: [10.1088/0004-637X/795/1/34](https://doi.org/10.1088/0004-637X/795/1/34)
- Skúladóttir, Á., Hansen, C. J., Salvadori, S., & Choplin, A. 2019, *A&A*, 631, A171, doi: [10.1051/0004-6361/201936125](https://doi.org/10.1051/0004-6361/201936125)
- Smith, V. V., Suntzeff, N. B., Cunha, K., et al. 2000, *AJ*, 119, 1239, doi: [10.1086/301276](https://doi.org/10.1086/301276)
- Sollima, A., Ferraro, F. R., Bellazzini, M., et al. 2007, *ApJ*, 654, 915, doi: [10.1086/509711](https://doi.org/10.1086/509711)
- Stanford, L. M., Da Costa, G. S., Norris, J. E., & Cannon, R. D. 2006, *ApJ*, 647, 1075, doi: [10.1086/505571](https://doi.org/10.1086/505571)
- Tailo, M., Di Criscienzo, M., D'Antona, F., Caloi, V., & Ventura, P. 2016, *MNRAS*, 457, 4525, doi: [10.1093/mnras/stw319](https://doi.org/10.1093/mnras/stw319)
- Ting, Y.-S., Conroy, C., Rix, H.-W., & Cargile, P. 2019, *ApJ*, 879, 69, doi: [10.3847/1538-4357/ab2331](https://doi.org/10.3847/1538-4357/ab2331)
- Ting, Y.-S., Rix, H.-W., Conroy, C., Ho, A. Y. Q., & Lin, J. 2017, *ApJL*, 849, L9, doi: [10.3847/2041-8213/aa921c](https://doi.org/10.3847/2041-8213/aa921c)
- Tiongco, M. A., Vesperini, E., & Varri, A. L. 2019, *MNRAS*, 487, 5535, doi: [10.1093/mnras/stz1595](https://doi.org/10.1093/mnras/stz1595)
- Tsuchiya, T., Dinescu, D. I., & Korchagin, V. I. 2003, *ApJL*, 589, L29, doi: [10.1086/375805](https://doi.org/10.1086/375805)
- Villanova, S., Geisler, D., Gratton, R. G., & Cassisi, S. 2014, *ApJ*, 791, 107, doi: [10.1088/0004-637X/791/2/107](https://doi.org/10.1088/0004-637X/791/2/107)
- Virtanen, P., Gommers, R., Oliphant, T. E., et al. 2020, *Nature Medicine*, 17, 261, doi: [10.1038/s41592-019-0686-2](https://doi.org/10.1038/s41592-019-0686-2)
- Wang, Z., Hayden, M. R., Sharma, S., et al. 2025a, arXiv e-prints, arXiv:2512.09527, doi: [10.48550/arXiv.2512.09527](https://doi.org/10.48550/arXiv.2512.09527)
- Wang, Z., Hayden, M. R., Sharma, S., et al. 2022, *MNRAS*, 514, 1034, doi: [10.1093/mnras/stac1425](https://doi.org/10.1093/mnras/stac1425)
- Wang, Z., Seth, A. C., Latour, M., et al. 2025b, *ApJ*, 994, 143, doi: [10.3847/1538-4357/ae102c](https://doi.org/10.3847/1538-4357/ae102c)
- Xiang, M., & Rix, H.-W. 2022, *Nature*, 603, 599, doi: [10.1038/s41586-022-04496-5](https://doi.org/10.1038/s41586-022-04496-5)
- Xiang, M., Ting, Y.-S., Rix, H.-W., et al. 2019, *ApJS*, 245, 34, doi: [10.3847/1538-4365/ab5364](https://doi.org/10.3847/1538-4365/ab5364)
- Zhao, G., Zhao, Y.-H., Chu, Y.-Q., Jing, Y.-P., & Deng, L.-C. 2012, *Research in Astronomy and Astrophysics*, 12, 723, doi: [10.1088/1674-4527/12/7/002](https://doi.org/10.1088/1674-4527/12/7/002)
- Ziliotto, T., Milone, A. P., Cordini, G., et al. 2025, arXiv e-prints, arXiv:2506.21187, doi: [10.48550/arXiv.2506.21187](https://doi.org/10.48550/arXiv.2506.21187)